

Stellar Migration and Chemical Enrichment in the Milky Way Disc: A Hybrid Model

James W. Johnson,¹★ David H. Weinberg,^{1,2,3} Fiorenzo Vincenzo,² Jonathan C. Bird,⁴ Sarah R. Loebman,⁵ Alyson Brooks,⁶ Thomas R. Quinn,⁷ Charlotte R. Christensen,⁸ et al.?

¹ Department of Astronomy, The Ohio State University, 140 W. 18th Ave., Columbus, OH, 43210, USA

² Center for Cosmology and Astroparticle Physics (CCAPP), The Ohio State University, 191 W. Woodruff Ave, Columbus, OH, 43210, USA

³ Institute for Advanced Study, 1 Einstein Dr., Princeton, NJ, 08540, USA

⁴ Department of Physics & Astronomy, Vanderbilt University, 2301 Vanderbilt Place, Nashville, TN, 37235, USA

⁵ Department of Physics, University of California Merced, 5200 North Lake Rd., Merced, CA, 95343, USA

⁶ Department of Physics & Astronomy, Rutgers University, 136 Frelinghuysen Rd, Piscataway, NJ, 08854, USA

⁷ Department of Astronomy, University of Washington, Box 351580, Seattle, WA, 98195, USA

⁸ Department of Physics, Grinnell College, 1116 8th Ave., Grinnell, IA, 50112, USA

Accepted XXX; Received YYY; in original form ZZZ

ABSTRACT

We investigate the impact of stellar migration on galactic chemical evolution models, considering a handful of assumptions for the star formation history and time-dependence of radial migration based on a zoom-in, hydrodynamical simulation of galaxy evolution. When stars migrate with a smooth, continuous time dependence, the type Ia supernova rate exhibits significant variability in our models. We demonstrate that this is a means with which young, super-solar $[\alpha/\text{Fe}]$ in the solar neighbourhood can arise naturally out of inside-out Galaxy growth with stellar migration. We find that the observed age- $[\alpha/\text{Fe}]$ relation is well-fit by an inside-out star formation history, while the age- $[\alpha/\text{H}]$ and age- $[\text{Fe}/\text{H}]$ relations are well-fit by a late starburst model; no one model investigated here fits both simultaneously. Our model successfully reproduces the broad nature of the $[\alpha/\text{Fe}]$ distribution at fixed $[\text{Fe}/\text{H}]$ in a given Galactic region; however, an overprediction of the frequency of intermediate $[\alpha/\text{Fe}]$ stars prevents it from explaining the observed results in detail. This suggests that inside-out galaxy growth combined with stellar migration, even with a late starburst, is not conducive to forming the infamous bimodality as it is observed. We postulate that more dramatic evolutionary scenarios (e.g. a two-infall model) may be necessary to describe the observed results. In conducting this analysis, we developed and made use of newly released features in the Versatile Integrator for Chemical Evolution (VICE) which are built to handle these models under a wide variety of assumptions. VICE is publicly available at <https://pypi.org/project/vice>.

Key words: methods: numerical – galaxies: abundances, evolution, star formation, stellar content

1 INTRODUCTION

The orbits of stars are not unchanging. While it has been known for some time that stars undergo radial migration (e.g. [Wielen, Fuchs & Dettbarn 1996](#); [Roškar et al. 2008a](#); [Loebman et al. 2011](#); [Minchev et al. 2012](#)), the true impact of this process on galactic chemical evolution (GCE) remains under debate. By mixing stellar populations which formed in Galactic regions with significantly different enrichment histories, in principle the impact could be considerable. While some authors argue that radial migration has only a small impact

on GCE (e.g. [Kubryk, Prantzos & Athanassoula 2013](#); [Khoperskov et al. 2021](#)), there are others who argue the contrary (e.g. [Schönrich & Binney 2009](#); [Sharma, Hayden & Bland-Hawthorn 2020](#)). Aside from the chemodynamical simulations involving N-body integrations (e.g. [Kubryk et al. 2013](#); [Vincenzo & Kobayashi 2020](#); [Khoperskov et al. 2021](#)), there are to date only a handful of GCE models that take this effect into account (e.g. [Matteucci & Francois 1989](#); [Schönrich & Binney 2009](#); [Minchev, Chiappini & Martig 2013](#); [Sharma et al. 2020](#)). These studies treat the Milky Way as a series of concentric annuli, each described by a conventional one-zone GCE model with parameters that change from annulus to annulus. In the resultant “multi-zone” model, stars and gas can

★ Contact e-mail: johnson.7419@osu.edu

migrate between zones under some prescription to account for time-dependent mixing processes. We retain such methodology in this paper, allowing star particles from a hydrodynamical simulation ran from cosmological initial conditions to inform our implemented mixing process; [Minchev et al. \(2013\)](#) employ a similar technique. With parameters tuned to reproduce certain observed results (e.g. abundance and surface density gradients), we can then assess the model predictions to address the following question: when combining simple, conventional assumptions about the star formation and dynamical histories of the Milky Way, what observed results can be replicated? In the present paper, we focus on the following observables: metallicity distributions functions (MDFs) and abundance gradients, the $[\alpha/\text{Fe}]$ bimodality, the age-metallicity relation (AMR), and the young, α -rich population.

Stars in the inner regions of the Milky Way tend to be more metal-rich than those found in the outskirts ([Nordström et al. 2004a](#); [Daflon et al. 2009](#); [Frinchaboy et al. 2013](#); [Hayden et al. 2014](#)), with slight variations in quantitative results based on what type of stars are considered and what metallicity tracers are analysed. Such behavior is also seen in the gas-phase gradients of low-redshift spirals (see, e.g., the results from the CHAOS project using HII regions; [Berg et al. 2015, 2020](#)). Using the 12th data release of the Apache Point Observatory Galaxy Evolution Experiment (APOGEE), [Hayden et al. \(2015\)](#) demonstrate that the observed MDF has a metal-rich mode and is skew-negative in the inner galaxy (and conversely, metal-poor and skew-positive in the outer galaxy). These variations in the skewness of the distributions with Galactocentric radius are usually attribute to the migration of metal-rich (metal-poor) stars from smaller (larger) orbital radii. Similar arguments are used by [Sellwood & Binney \(2002\)](#) to interpret the results of [Edvardsson et al. \(1993\)](#) on scatter in the age-metallicity relation observed in the solar neighbourhood.

Abundance gradients have been the focus of many studies and are quantified rather extensively, but their origin is somewhat up for debate. Applying the analytic models of [Weinberg, Andrews & Freudenburg \(2017\)](#), one could argue that the gradient arises out of variations in the local gas-phase equilibrium abundance as a function of Galactocentric radius. For α -elements, the equilibrium abundance is determined to first order by their yield and the efficiency of outflows in removing metals from the star forming reservoir. With a stronger gravitational potential in the inner regions of the Galaxy, one might reasonably expect outflows to be weaker there, thereby increasing the equilibrium abundance. [Nidever et al. \(2014\)](#) used such an approach to reproduce the width of the $[\text{Fe}/\text{H}]$ distribution for low- α sequence stars in APOGEE. However, recent chemical evolution models have successfully replicated the gradient with no outflowing winds at all (e.g. [Minchev et al. 2013](#); [Spitoni et al. 2019](#)). This is based on arguments from [Melioli et al. \(2008, 2009\)](#), [Spitoni, Recchi & Matteucci \(2008\)](#), and [Spitoni et al. \(2009\)](#) who studied Galactic fountains using hydrodynamical simulations and numerical models, finding that ejected metals tend to reaccrete to a Galactocentric radius similar to where they originated. With this result, some authors argue that such outflows do not significantly alter the chemical evolution of a Galactic disc, and that instead the gradient arises from the higher normalization of the star formation history in the inner Galaxy.

Like radial abundance gradients, the reality of the infamous $[\alpha/\text{Fe}]$ dichotomy is well established (in Gaia-ESO: [Recio-Blanco et al. 2014](#); [Rojas-Arriagada et al. 2017](#); in APOGEE: [Nidever et al. 2014](#); [Hayden et al. 2015](#); [Weinberg et al. 2019](#)), but its origin is a topic of intense debate. In general, stars in the Milky Way tend to fall in one of two populations - the roughly solar $[\text{Fe}/\text{H}]$, solar $[\alpha/\text{Fe}]$

stars commonly referred to as the low- α sequence, and the high- α sequence made up of sub-solar $[\text{Fe}/\text{H}]$, super-solar $[\alpha/\text{Fe}]$ stars. Recently explored with more current data by [Sharma et al. \(2020\)](#), the notion that it could in principle arise out of radial migration traces back to [Schönrich & Binney \(2009\)](#). Applying the analytic models of [Weinberg et al. \(2017\)](#), an alternative pathway to such abundance patterns is by an increase in the strength of outflows at late times. Such an evolutionary model would predict a decrease in the equilibrium abundance, forming stars along the low- α sequence. This scenario has not yet been explored in combination with radial migration.

Other authors argue that more dramatic evolutionary events are necessary to explain the observed results, such as the two-infall model ([Chiappini, Matteucci & Gratton 1997](#); [Chiappini, Matteucci & Romano 2001](#); [Romano et al. 2010](#); [Grisoni et al. 2017](#); [Noguchi 2018](#); [Palla et al. 2020](#); [Spitoni et al. 2016, 2018](#)). In these models, the high- α sequence forms during the Galaxy's initial collapse before feedback processes shut off star formation and expel gas into the Galactic halo. Then, this material can cool and reaccrete along with additional, metal-poor gas from the intergalactic medium, producing a second episode of star formation. The dilution associated with the second accretion event lowers the gas-phase Fe abundance at fixed $[\alpha/\text{Fe}]$, forming stars along the low- α sequence. [Spitoni et al. \(2019, 2020\)](#) demonstrated using the APOKASC sample ([Pinsonneault et al. 2014](#); [Silva Aguirre et al. 2018](#)) that such models can explain the abundances observed in the solar annulus. Although [Spitoni et al. \(2021\)](#) recently extended this model to Galactic regions beyond the solar annulus, their model did not account for the mixing of stellar populations between regions. Though they invoke [Kubryk et al. \(2013\)](#) and [Khoperskov et al. \(2021\)](#) as arguments that it shouldn't impact their results, this nonetheless means that two-infall models have not yet been explored in combination with a treatment for stellar migration.

Recent cosmological zoom-in simulations have found results qualitatively similar to the arguments of [Spitoni et al. \(2019, 2020, 2021\)](#). Using the Auriga simulation suite ([Grand et al. 2017](#)), [Grand et al. \(2018\)](#) demonstrate that an early, accretion induced starburst can populate the high- α sequence, followed by low-level, sustained star formation on the low- α sequence. In this pathway, there is either a rapid transition between the two phases, ensuring the chemical space between the sequences is relatively unpopulated, or low-metallicity gas accretion dilutes the star forming reservoir at fixed $[\alpha/\text{Fe}]$, populating the low $[\text{Fe}/\text{H}]$, low $[\alpha/\text{Fe}]$ portion of the low- α sequence. [Buck \(2020\)](#) finds the dilution scenario in the NIHAO simulation suite as well ([Wang et al. 2015](#); [Buck et al. 2020](#)). Although the [Spitoni et al. \(2021\)](#) model did not implement mixing of stellar populations, these studies using hydrodynamical simulations would suggest pathways qualitatively similar to their two-infall model.

Contrary to this scenario, [Clarke et al. \(2019\)](#) demonstrate that star formation proceeded in clumps in an SPH simulation using GASOLINE ([Wadsley, Keller & Quinn 2017](#)). These clumps self-enrich, forming stars on the high- α sequence due to the perturbed ratio of core collapse to type Ia supernova rates within the star forming regions. The more spatially extended, smooth star formation populates the low- α sequence. Suffice it to say that there are no shortage of models which reproduce the dichotomy, but only those done with hydrodynamical simulations and a handful of others (e.g. [Schönrich & Binney 2009](#); [Minchev et al. 2013](#); [Sharma et al. 2020](#)) have taken into account stellar migration.

Besides abundance gradients and the $[\alpha/\text{Fe}]$ dichotomy, another observable of interest in this paper is the age-metallicity rela-

tion (AMR): the correlation between stellar ages and metallicities. The observed AMR in the solar neighbourhood is known to exhibit considerable intrinsic scatter (Edvardsson et al. 1993); this is usually attributed to radial migration of metal-rich (metal-poor) stars from smaller (larger) Galactocentric radii (Sellwood & Binney 2002; Haywood 2008; Roškar et al. 2008b; Schönrich & Binney 2009). In the solar neighbourhood, Feuillet et al. (2018) reveal that super-solar metallicity stars are statistically older than solar metallicity stars (see their Fig. 3). This contrasts with the predictions of simple one-zone models of GCE where enrichment proceeds alongside star formation, yielding a monotonic AMR (e.g. Andrews et al. 2017; Weinberg et al. 2017). Although one-zone models of starbursts can predict a non-monotonic AMR due to the effect of dilution (Johnson & Weinberg 2020), by construction they do not predict multiple abundances at fixed age as Feuillet et al. (2018) reports. Using the Weinberg et al. (2017) analytic models, Feuillet et al. (2018) argues that this is a consequence of radial migration. For a smooth star formation history, the youngest stars at a given radius will have compositions reflective of the local equilibrium abundance; only stars born at different radii will have different compositions, and only the old ones will have had time to migration to the solar annulus.

While the presence of old-metal rich stars in the solar annulus is peculiar because they are at odds with one-zone models of chemical evolution, the presence of young, α -rich stars is interesting for the same reason. For a smooth star formation history, the delayed nature of type Ia supernovae and their Fe production cause $[\alpha/\text{Fe}]$ to decrease with time, predicting an age- $[\alpha/\text{Fe}]$ relation that should increase monotonically with stellar age. However, these \sim few Gyr old stars with $[\alpha/\text{Fe}] \approx +0.1 - 0.2$ stars have been found using stellar ages estimated from carbon-to-nitrogen ratios (Martig et al. 2016), isochrone matching (Feuillet et al. 2018, 2019), and with the asteroseismic ages of the original APOKASC catalog (Chiappini et al. 2015; Silva Aguirre et al. 2018; Pinsonneault et al. 2014). Silva Aguirre et al. (2018) demonstrate that these stars have kinematics similar to the rest of the high- α population, postulating that they may be the consequence of stellar mergers or mass transfer events, making truly old stars simply appear younger. In a sample of 51 young, α -enhanced red giant stars, Hekker & Johnson (2019) conclude that a portion of these stars have carbon-to-nitrogen ratios consistent with mass transfer events, but that this cannot account for the entire population. This suggests that the remaining stars are either truly young or the result of mergers on the main sequence. If not, then a theoretical explanation for the origin of these stars remains a mystery.

Alternatively, a recent starburst event could have produced these stars. Mor et al. (2019) infer a factor of ~ 2 enhancement in the star formation history (SFH) of the Milky Way ~ 2 Gyr ago by comparing population synthesis models to observed stellar luminosity functions and colour-magnitude diagrams from Gaia data (Gaia Collaboration et al. 2018). Isern (2019) reach similar conclusions by modeling the white dwarf luminosity function in the solar neighbourhood with Gaia parallaxes. Motivated by these results, Johnson & Weinberg (2020) demonstrate using one-zone chemical evolution models that a recent starburst of this nature can produce similarly young, α -rich stars. However, the caveat to this interpretation is that the starburst must be sufficiently localized such that the resultant stellar populations remain outliers from an otherwise monotonically increasing age- $[\alpha/\text{Fe}]$ relation.

The impact of such evolutionary histories combined with stellar migration is, to our knowledge, yet unexplored in the literature. A viable model for the detailed enrichment history of the Milky Way

would simultaneously explain all of these observed results and their variations between Galactic regions, while also taking into account effects like mixing and observational systematics. On top of this, it must self-consistently calculate enrichment rates from adopted nucleosynthetic yields and the SFH. In this paper, we aim to assess the extent to which conventional assumptions about the evolutionary history of the Milky Way can account for these results, entertaining a handful of assumptions describing the SFH and time-dependence of stellar radial migration.

Motivated by the general result that galaxies grow in radius with time (i.e. “inside-out” growth; Bird et al. 2013), our base-line model has a star formation history (SFH) whose e-folding timescales grow with Galactocentric radius. Based on the findings of Mor et al. (2019) and Isern (2019), we also construct models in which a late starburst is imposed atop the inside-out SFH. In one model, this starburst occurs in all annuli, and in another, loosely informed by the findings of Vincenzo & Kobayashi (2020) suggesting such a radial dependence to accretion, it occurs only at ≥ 6 kpc. We also construct a model in which the SFH is constant at a given Galactocentric radius; these models are interesting from a theoretical perspective in that they quantify the impact of stellar migration without the effects of a time-dependent SFH.

2 METHODS

To fulfill the goals of this paper, we develop and make use of newly released features within the *Versatile Integrator for Chemical Evolution* (VICE; Johnson & Weinberg 2020). These features are designed to handle models such as these with a wide range of flexibility. We reserve a description of VICE’s migration algorithm and our simulation parameters for §2.2, first describing our sample of star particles from the hydrodynamical simulation.

Although we make use of a hydrodynamical simulation to drive stellar migration, we do *not* make use of its SFH. While our study employs similar techniques as Minchev et al. (2013), our differs in this subtle aspect. An alternative to modeling radial migration based on a hydrodynamical simulation is to invoke dynamical arguments; Schönrich & Binney (2009) and Sharma et al. (2020) take such an approach. This method, however, introduces free parameters which then require fitting to data. An advantage of our technique is that there are no free parameters introduced to the model; furthermore, it’s unclear the extent to which the fit biases the model into agreement with parts of the data not involved in the fitting process. The dynamical history of a hydrodynamical simulation is also motivated by first principles in that it models gravitational interactions via an N-body integration. The primary disadvantage of this approach is a consequence of the lack of free parameters - the model is rigid, and we cannot explore slight variations. However, in principle one could compare the predictions made by our chemical evolution models when ran using different hydrodynamical simulations. We emphasize that a hydrodynamical simulation *only* informs the mixing processes in our models, and there is no N-body integration involved in our models aside from that which was used to run the hydrodynamical simulation in the first place.

2.1 The Hydrodynamical Simulation

In this paper we make use of star particles from the h277 simulation (Christensen et al. 2012; Zolotov et al. 2012; Loebman et al. 2012, 2014; Brooks & Zolotov 2014). Recently employed to study the stellar age-velocity relationship, a synopsis of its detailed simulation

parameters and cosmological model can found in §2 of [Bird et al. \(2020\)](#). We do not include any discussion of these details here, instead focusing on how we vet the sample of star particles for use in our chemical evolution models.

It is of particular important to have accurately measured formation radii for each star particle that we use in our analysis. h277 did not record the exact birth radius of each star particle; however, each star particle does have an accurate age at each snapshot. Since stellar orbits are unlikely to change significantly in an adequately short time interval, the radii of sufficiently young stars in their first snapshot are reasonable approximations of their birth radii. We therefore restrict our sample to those with an age at first snapshot of ≤ 150 Myr, and adopt their Galactocentric radius at that time as their birth radius. We have also conducted this analysis with a maximum age at first snapshot of 50 Myr, and found similar results, suggesting that these time intervals are short enough to not impact our conclusions. In practice, we find that 150 Myr also provides with an adequately large number of star particles to sample from. Of the star particles that remain after imposing this cut, the oldest one is 12.26 Gyr old at the present day. Our model can only apply on timescales as long as or shorter than the full range of ages of the sample of star particles; we therefore subtract 1.5 Gyr from the formation times of all star particles, allowing $T = 0$ in our models to correspond to $T = 1.5$ Gyr in h277. As a consequence, our disc models trace the chemical evolution of the Galaxy out to a lookback time of ~ 12.2 Gyr, or a redshift of $z \approx 3$, placing the onset of star formation at that time.

We further restrict our sample of star particles to only those with both formation and final radii of $R_{\text{gal}} \leq 20$ kpc, and to have formed within $|z| \leq 3$ kpc of the disc midplane. These criteria ensure that we're only using star particles which formed in-situ. While it's possible that some star particles formed in a dwarf galaxy as it was infalling, a scenario which would satisfy these requirements, these star particles are few in number, and are only relevant at large R_{gal} and high ages - a region of parameter space where few stars form anyway.

Based on a kinematic decomposition performed on the present-day phase space distribution of the h277 star particles, we include all those with bulge, pseudobulge, and disc-like kinematics, excluding halo stars. While we're not modeling the evolution of the bulge here, these star particles are overwhelmingly located at $R_{\text{gal}} \leq 3$ kpc at the present day anyway; here we're much more interested in $R_{\text{gal}} \geq 3$ kpc since we're modeling the evolution of the disc. These cuts yield a sample of 3,000,556 star particles from h277.

h277 had a transient bar during its evolution, but does not have one at $z = 0$ ([citation?](#)). This is a noteworthy difference between our model and that of [Minchev et al. \(2013\)](#), and by extension the [Minchev, Chiappini & Martig \(2014\)](#) and [Minchev et al. \(2017\)](#) studies which use it as well, because they selected a hydrodynamical simulation of a galaxy specifically so that it would have a strong bar at $z = 0$; the transient bar in h277 was not strong. This could mean that the dynamical history of our model Galaxy does not reflect that of [Minchev et al. \(2013\)](#) and perhaps the Milky Way itself. However, the difference is likely within the uncertainties of the current understanding of the Milky Way's dynamical history. Although an investigation on the impact of bar evolution on stellar migration and thus chemical evolution is outside the scope of this paper, it is an interesting question which can be probed by simply swapping the h277 data within VICE for another simulation, then rerunning our numerical models and comparing the results.

In the top row of Fig. 1, we plot the distributions of final radius in bins of birth radius and age for our sample of star particles. Conversely, the bottom rows distributions of birth radii in bins of final

radius and age. Focusing on the top row of panels, we note that for star particles born at any radius and time, the distribution of final radius is still peaked near the birth radius, but moves slightly inward with increasing age. The tails of the distributions toward larger R_{gal} are nearly age-independent, while the tails toward smaller R_{gal} are not. This suggests that radial migration inward and outward occur on different timescales in h277, specifically that inward migration is slower than outward migration. By extension, this suggests that the two may be tied to different physical processes. In a cosmological simulation, [Roškar et al. \(2008a\)](#) demonstrate that resonant scattering at corotation causes stars to move outward and gas to move inward. It's possible that stellar migration inward has different origins.

Focusing on the bottom row of panels in Fig. 1, we note that the mode of the birth radius distributions show a stronger dependence on age than the mode of the final radius distributions. At any Galactocentric radius at the present day, the youngest stars are overwhelmingly born at comparable radii, while the oldest stars are overwhelmingly born at smaller radii. This is most noticeable in at large R_{gal} . The differences between the two can be understood by considering the steep nature of the radial gradient in stellar surface density. Take for example the 8 - 10 Gyr age bin in both $R_{\text{Birth}} = 5 - 7$ kpc and $R_{\text{Final}} = 11 - 13$ kpc bins (i.e. the red curves in the top-left and bottom-right panels). For these old stars born at 5 - 7 kpc, 11 - 13 kpc is far down the tail of the R_{Final} distribution, and yet 5 - 7 kpc is the mode R_{Birth} of all old stars presently at these radii. This implies that even though a plurality of 8 - 10 Gyr old stars with $R_{\text{Final}} = 11 - 13$ kpc were born at 5 - 7 kpc, they account for only a small fraction of the stars with similar birth radii. This is only possible if there are many more stars born at small R_{gal} than large R_{gal} , implying a stellar surface density which decreases as a strong function of Galactocentric radius. This is known to be the case (e.g. [Bland-Hawthorn & Gerhard 2016](#)).

We also note that the top row of Fig. 1 demonstrates that the number of stars which migrated inward and outward are comparable in h277. In fact, taking $|\Delta R_{\text{gal}}| \geq 500$ pc between birth and final radii as the criterion for migration inward or outward, we indeed find as global percentages in our sample that 27% migrated inward, 29% migrated outward, and the remaining 44% stayed near their birth radius. Furthermore, these distributions contain some information on the timescales of radial migration. In all bins of birth radius, a good first-order estimate of the probability density that a star has a final radius in the same bin is ~ 0.3 . With bins in birth radius of 2 kpc, this suggests that only $\sim 60\%$ of stars remain in their birth radius bin by the time their ~ 2 Gyr old, and the remaining $\sim 40\%$ have migrated already. If the type Ia supernova delay-time distribution (SN Ia DTD) is a $t^{-1.1} \approx t^{-1}$ power-law as suggested by observational results (e.g. [Maoz & Mannucci 2012](#); [Maoz & Graur 2017](#)), then we expect similar numbers of SN Ia events to occur with delay times between 1 and 10 Gyr as we do between 100 Myr and 1 Gyr. With such an extended DTD, and the timescales for migration implied by Fig. 1, it's possible that SN Ia progenitors can migrate significant distances before exploding. Indeed, in the ASAS-SN bright SN catalog, $\sim 10\%$ of SNe are seen at >10 kpc from their host galaxies ([Holoien et al. 2019](#)). While this catalog is for *all* supernovae seen by ASAS-SN, the majority of SN events are type Ia anyway. Based on this, it's reasonable to expect that the migration of nucleosynthetic may proceed alongside stellar migration. This effect has largely been neglected by GCE studies to date on the grounds that radial migration is a slow process, and thus the majority of nucleosynthesis should occur near a star's birth radius (e.g. [Minchev et al. 2013](#), and in the application of the [Weinberg et al. 2017](#) analytic models

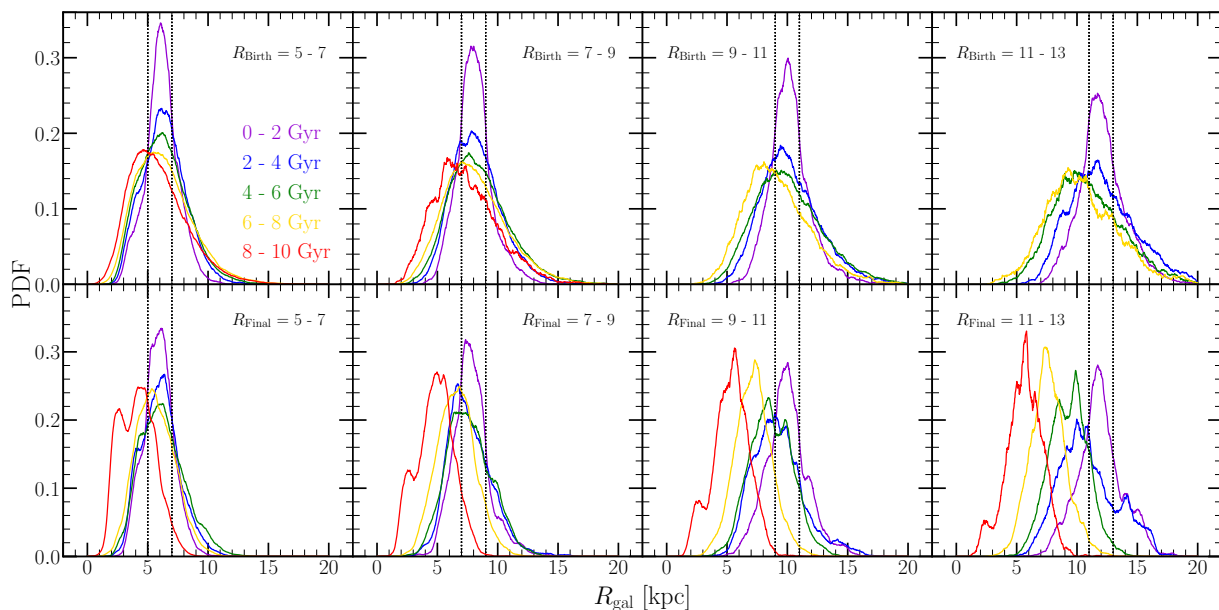


Figure 1. Radial distributions of our star particles from h277. In the top row, we show distributions of *final* radius in bins of birth radius and age, and in the bottom row, we show distributions of *birth* radius in bins of final radius and age. Each bin in Galactocentric radius is shown in its own panel, denoted in text at the top of each panel and by vertical black dashed lines. We colour-code the distributions according to the age of the star particles, denoted by the legend in the upper left panel. We smooth all distributions with a box-car width of 0.5 kpc to improve clarity. We omit the distributions for 8 - 10 Gyr old stars born in the 9 - 11 and 11 - 13 kpc bins due to an insufficient number of star particles with which to calculate the distribution.

in Feuillet et al. 2018). However, with the realization that the SN Ia duty cycle is also a slow process due to the long tail of the DTD, it is possible that stellar migration and SN Ia occur on similar timescales. Therefore, we relax this assumption in the present paper. We discuss the application of the h277 star particle data to our model for radial migration and the time dependence thereof in the next section.

2.2 Radial Migration

As in previous studies (e.g. Schönrich & Binney 2009; Minchev et al. 2013; Sharma et al. 2020), in this paper we model the Milky Way as a series of concentric annuli with a uniform width ΔR_{gal} . To run numerical simulations of these models, we develop and make use of VICE’s `milkyway` object, designed specifically for such an approach. The `milkyway` object is a subclass of a more general object named `multizone`; at its core a `multizone` object is an array of `singlezone` objects, which are designed to handle one-zone models of GCE and were the focus of Johnson & Weinberg (2020), VICE’s initial release paper. The `multizone` object affords users full control over which zone any individual stellar population is in at all timesteps following its formation as well as the ability to move gas between any two zones with any time dependence. In principle this should allow for arbitrarily complex zone configurations and migration prescriptions. The `milkyway` object is a user-friendly extension of this which enforces an annular zone configuration as we take here. As defaults, it adopts the stellar migration model detailed in this section and our star formation law discussed in § 2.5.

As in hydrodynamical simulations, stars in VICE are stand-ins for entire stellar populations. They’re said to be in a given zone if their radius is between the inner and outer edges of the annulus. At all times, their nucleosynthetic products and returned envelopes are placed in the ISM of the annulus that they are in *at that time*. Where hydrodynamical and N-body simulations of Galaxy evolution tend

to use star particles of a fixed mass, however, VICE forms a fixed number of stellar populations per zone per timestep, and allows their masses to vary to account for variations in the star formation rate (SFR). The mass of stars formed in a given zone is divided evenly among the stellar populations that form in a given zone and timestep.

The final radius of a stellar population is then determined based on the birth and final radii of star particles in a hydrodynamical simulation, for which we’ve taken h277 in this paper (see discussion in §2.1). Describing the Galaxy as a series of concentric annuli, VICE’s `milkyway` object assumes stellar populations are born at the centres of each annulus. For a stellar population born at a time T and Galactocentric radius R_{gal} , it first searches for star particles from h277 that formed at $T \pm 250$ Myr and $R_{\text{gal}} \pm 250$ pc. It then randomly selects a star particle from this subsample with no bias to act as an *analog*. This stellar population then assumes the change in orbital radius ΔR_{gal} of its analog at face value, and moves from its birth radius to the implied final radius at $T = 12.2$ Gyr with an assumed time dependence. If no candidate analogs are found, VICE widens the search to $T \pm 500$ Myr and $R_{\text{gal}} \pm 500$ pc. If still no analog is found, then it finds the star particle with the smallest difference in birth radius still within a birth time of $T \pm 500$ Myr, and assigns it as the analog. While this prescription allows stellar populations to be assigned analogs with significantly different birth radii, this is only an issue for small T and large R_{gal} where there are few star particles from h277, and where few stars form in nature anyway due to the inside-out growth of galaxies (Bird et al. 2013). Furthermore, due to the similarity of the histograms in the top row of Fig. 1, we expect taking ΔR_{gal} from a star particle which formed at a similar time but different birth radius in these instance to be accurate enough for our purposes.

Our models assume that the Galaxy is vertically and azimuthally well-mixed, and that the radial direction is the only one

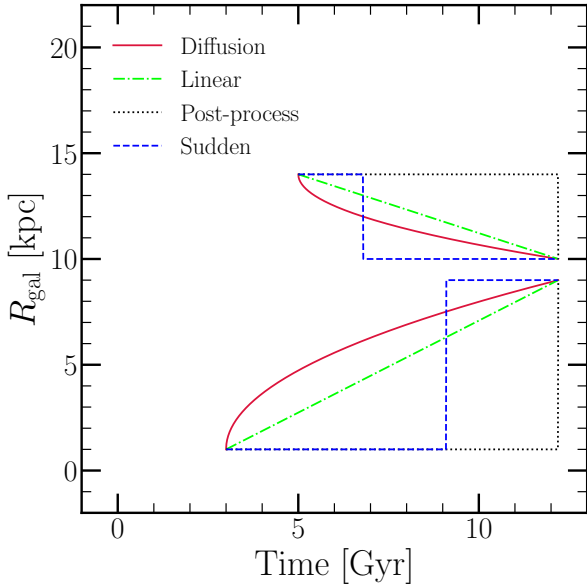


Figure 2. A diagram illustrating how Galactocentric radius changes with time for two stellar populations under our migration schema: diffusion (crimson, solid), linear (lime, dot-dashed), post-process (black, dotted), and sudden (blue, dashed). Here the initial and final radii and birth times are chosen at random for illustrative purposes. With the initial and final Galactocentric radii of a stellar population, its birth time, and one of these assumptions regarding the time-dependence of radial migration, the Galactocentric radius at all times is known.

in which there are significant differences in composition. That is, each annulus extends from the disc midplane at $z = 0$ to $z = \pm\infty$, and whether or not a star particle is in a given annulus does not depend on z at all. In fact, this information is *not* used in integrating our models with VICE. Instead, we simply assume that each stellar population in our models are located at the present day z_{final} of its assigned analog. Furthermore, when an h277 star particle is assigned as an analog, it is *not* thrown out of the sample of candidate analogs, in theory allowing a star particle to act as an analog for multiple stellar populations. This is a subtle difference between the Minchev et al. (2013) model and ours; where we assign star particles to stellar populations for which VICE then calculates a stellar mass and composition based on an assumed SFH, the Minchev et al. (2013) uses a chemical evolution model to assign compositions to star particles.

With a known birth radius and time from our GCE model and an implied ΔR_{gal} from a stellar population’s assigned analog, the final radius is known and the only missing piece of information is the time-dependence with which it moves there. In the present paper we consider four parameterized assumptions to describe this, each of which are illustrated conceptually in Fig. 2.

- **Post-Processing:** Stars stay where they are born until the final timestep, at which point they instantly migrate to their final radius. This retains the assumption that stars do not contribute to nucleosynthesis beyond their birth radius as employed in previous studies (e.g. Minchev et al. 2013). In this scenario, each annulus is treated as a one-zone model independent of all other zones. We illustrate this case with a black dotted line in Fig. 2.

- **Sudden:** A random number is drawn from a uniform distribution between a stellar population’s time of birth and the present day. That time is taken to be the time of instantaneous migration

to the present-day annulus. This emulates a scenario in which a single dynamical interaction changes a star’s orbital radius, and be thought of mathematically as a time-dependent extension of the post-processing scenario. We illustrate this case with a blue dashed line in Fig. 2.

- **Diffusion:** Stars move to their final radii in a continuous, time-dependent manner in this case. So named because it corresponds to a scenario in which angular momentum diffuses via a random walk, under this assumption, the mean displacement of stars that migrate similar distances would scale with $\sqrt{\text{age}}$. This is our fiducial migration model, and we present results with this assumption unless otherwise noted. This is qualitatively similar to Frankel et al. (2018, 2020), who also model radial orbit migration with a \sqrt{t} dependence. We illustrate this case with a red solid line in Fig. 2.

- **Linear:** A simple variation of the diffusion model in which the migration to the final radius scales linearly with age rather than with $\sqrt{\text{age}}$. There is no physical motivation for this model other than mathematical ease, but together with the diffusion model it constitutes a test of how sensitive our conclusions are to the time-dependence of stellar migration. We illustrate this case with a green dot-dashed line in Fig. 2.

In all models, we neglect radial gas flows (Lacey & Fall 1985; Bilitewski & Schönrich 2012), instead focusing on these simple assumptions describing how orbital radii change with time. While such an investigation would be an interesting extension of our study, we reserve it for future work.

We emphasize that there is *no* N-body integration employed in our models aside from that which ran the h277 simulation. Furthermore, we use our sample of analog star particles from it *only* in determining ΔR_{gal} of each of our model stellar populations (see discussion in § 2.1). While h277 had its own SFH and chemical enrichment history, we make use of neither of these components here; rather, these are exactly what we seek to explore variations of. We acknowledge that stellar migration is often formulated using the processes “blurring” and “churning”, referring to a star’s epicyclic motions and changes in the guiding center of its orbit (e.g. Sellwood & Binney 2002; Schönrich & Binney 2009; Minchev et al. 2011); migration can also occur due to the overlap of spiral arm and bar resonances in the disc (Minchev et al. 2011). We refrain from discussion of this approach here, because our models do not make use of such methodology. In the present paper, the orbital radii at all times are calculated and assumed at face value given one of the four assumptions detailed in the bullet list above.

2.3 Nucleosynthetic Yields, Outflows, and Recycling

Nucleosynthesis proceeds in our models according to *fractional net* yields, as required by VICE. That is, our yields quantify the mass of some element x ejected to the interstellar medium (ISM) in units of the progenitor stellar population’s total initial mass, and only accounts for *newly produced* nucleosynthetic material. VICE takes into account the return of previously produced nucleosynthetic products with a separate implementation. In the present paper, we focus our analysis on alpha and iron-peak elements, taking oxygen (O) and iron (Fe) as the representative cases. The dominant enrichment channels of interest in our models are thus core collapse and type Ia supernovae (Johnson 2019). Though we choose O and Fe, we expect similar results to be found for other alpha (e.g. Ne, Mg, Si) and iron-peak elements (e.g. Mn, Ni, Co), with purely quantitative differences reflective of the relative yields between elements.

Enrichment from core collapse supernovae (CCSNe) happens

immediately following the formation of progenitor stars in VICE. This is an adequate approximation, because the lifetimes of massive stars are short compared to the relevant timescales for galaxy evolution. For the most massive stars, the lifetimes are comparable to the timestep size we adopt in this paper anyway. This assumption implies a linear relationship between the CCSN enrichment rate and the SFR:

$$\dot{M}_x^{\text{CC}} = y_x^{\text{CC}} \dot{M}_\star \quad (1)$$

where y_x^{CC} is the CCSN yield of some element x . Physically, this quantity represents the mass of an element x ejected to the interstellar medium (ISM) from all CCSNe events associated with a stellar population in units of the stellar population's initial mass. For example, if $y_x^{\text{CC}} = 0.01$, a hypothetical $100 M_\odot$ stellar population would add $1 M_\odot$ of x to the ISM immediately. This procedure neglects the mass that would be lost to outflows, which like recycling, have a separate implementation in VICE. In this paper, we adopt $y_{\text{O}}^{\text{CC}} = 0.015$ and $y_{\text{Fe}}^{\text{CC}} = 0.0012$ from Johnson & Weinberg (2020), who in turn adopt these values from Weinberg et al. (2017).

SN Ia nucleosynthesis products are injected according to a $t^{-1.1}$ DTD with a minimum delay time of $t_D = 150$ Myr. This is the default DTD in VICE, which was also adopted by Johnson & Weinberg (2020), and is suggested by recent observational results comparing the cosmic SN Ia rate to the cosmic SFH (Maoz & Mannucci 2012; Maoz & Graur 2017). In a one-zone model at times $t > t_D$, the enrichment rate of some element x can be expressed as the product of some yield y_x^{Ia} and the SFH weighted by the DTD:

$$\dot{M}_x^{\text{Ia}} = y_x^{\text{Ia}} \langle \dot{M}_\star \rangle_{\text{Ia}} \quad (2a)$$

$$= y_x^{\text{Ia}} \frac{\int_0^{t-t_D} \dot{M}_\star(t') R_{\text{Ia}}(t-t') dt'}{\int_{t_D}^{t_{\text{max}}} R_{\text{Ia}}(t') dt'} \quad (2b)$$

where R_{Ia} is the DTD itself, which has units of $M_\odot^{-1} \text{Gyr}^{-1}$. Like the CCSN yield, y_x^{Ia} is the mass of some element x produced over the SN Ia duty cycle in units of the progenitor stellar population's initial mass. It can also be expressed as an integral over the DTD:

$$y_x^{\text{Ia}} = m_x^{\text{Ia}} \int_{t_D}^{t_{\text{max}}} R_{\text{Ia}}(t') dt' = m_x^{\text{Ia}} \frac{N_{\text{Ia}}}{M_\star} \quad (3)$$

where m_x^{Ia} is the average mass of the element x produced in a single SN Ia event and the integral evaluates to the mean number of SN Ia events N_{Ia} per mass of stars formed M_\star . VICE forces $t_{\text{max}} = 15$ Gyr always, though provided one is consistent with equations (2b) and (3), the results are independent of t_{max} since the integrals cancel.

Extending this formalism to multi-zone models is simple - rather than an integral over the star formation history of a given annulus, the rate becomes a summation over all stellar populations that are in a given zone at some time:

$$\dot{M}_x^{\text{Ia}} = y_x^{\text{Ia}} \frac{\sum_i M_i R_{\text{Ia}}(\tau_i)}{\int_{t_D}^{t_{\text{max}}} R_{\text{Ia}}(t') dt'} \quad (4)$$

where M_i and τ_i are the mass and age of the i 'th stellar population, respectively.

Initially, we adopt $y_{\text{O}}^{\text{Ia}} = 0$ and $y_{\text{Fe}}^{\text{Ia}} = 0.0017$ from Johnson & Weinberg (2020), who in turn adopt these values from Weinberg et al. (2017). However, in practice we find that the e-folding

timescales of star formation in our models are sufficiently long (see discussion in § 2.4) such that our fiducial, inside-out SFH model predicts $[\text{O}/\text{Fe}] \approx +0.05$ for young stars. We therefore multiply $y_{\text{Fe}}^{\text{Ia}}$ by $10^{0.1}$, adopting instead $y_{\text{Fe}}^{\text{Ia}} = 0.00214$ in order for our fiducial model to predict a late-time $[\text{O}/\text{Fe}]$ ratio in better agreement with observations. Although there is no motivation for such a change aside from this, this decision is likely within the uncertainties in SN Ia nucleosynthetic yields anyway.

Our models assume that all supernova yields of O and Fe are independent of metallicity. While this appears to be empirically true in the Milky Way for O and Fe (Weinberg et al. 2019; Griffith, Johnson & Weinberg 2019; Griffith et al. 2020), our CCSN yields are based on supernova explosion models in which all $>8 M_\odot$ progenitors produce a CCSN event (e.g. Chieffi & Limongi 2004, 2013). Recent findings with regard to black hole formation and stellar explosability have demonstrated that many massive stars instead collapse directly to a black hole (see theoretical discussion by, e.g., Pejcha & Thompson 2015; Sukhbold et al. 2016; Ertl et al. 2016, and observational evidence from Gerke, Kochanek & Stanek 2015; Adams et al. 2017; Basinger et al. 2020). Such effects would necessarily lower CCSN yields of all elements. While VICE includes functionality with which to calculate y_x^{CC} for some element x using built-in tables from supernova nucleosynthesis studies, an in-depth investigation of the impact of these effects is outside the scope of this paper. Such an investigation which expands the capabilities of VICE will be presented in Griffith et al. (2021, in prep).

With regard to our SN Ia yields, Brown et al. (2019) demonstrate that the local specific SN Ia rate shows a strong, inverse dependence on galaxy stellar mass. They argue that this may imply a metallicity dependent R_{Ia} that produces more SN Ia events at early times when the metallicity is low. However, these metallicity are only present in our models at very early times. Furthermore, when outflows are taken into account, these yields are known to predict observationally plausible abundances (Andrews et al. 2017; Weinberg et al. 2017). We find similar results in our models.

Weinberg et al. (2017) demonstrate that, to first order, the nucleosynthetic yields of a given element and the strength of outflowing winds determine the late-time equilibrium abundance in the ISM. We retain their characterization of outflows here, in terms of a mass-loading factor η describing the ratio of the mass outflow to the SFR:

$$\eta \equiv \frac{\dot{M}_{\text{out}}}{\dot{M}_\star} \quad (5)$$

Here we adopt a scaling of η with R_{gal} such that the late-time equilibrium abundance as a function of radius describes a metallicity gradient in agreement with observations; Nidever et al. (2014) employ a similar methodology.

The procedure outlined here makes two assumptions: 1) that the equilibrium abundance at a given radius corresponds to the mode of the observed MDF, and 2) that radial migration does not significantly alter the overall form of the gradient. We demonstrate that this holds in our models in §3.1. For alpha elements, Weinberg et al. (2017) defines the equilibrium abundance under a constant SFH as:

$$Z_{\alpha, \text{eq}} = \frac{y_\alpha^{\text{CC}}}{1 + \eta(R_{\text{gal}}) - r} \quad (6)$$

where r is the recycling parameter (≈ 0.4 for the sake of this scaling with a Kroupa 2001 IMF; see discussion in § 2.2 of Weinberg et al.

2017). Solving for $\eta(R_{\text{gal}})$ yields:

$$\eta(R_{\text{gal}}) = \frac{y_{\alpha}^{\text{CC}}}{Z_{\alpha, \text{eq}}} + r - 1 = \frac{y_{\alpha}^{\text{CC}}}{Z_{\alpha, \odot}} 10^{-\text{mode}([\alpha/\text{H}]) (R_{\text{gal}})} + r - 1 \quad (7)$$

The metallicity gradient in the Milky Way has been the focus of a number of studies to date. Nordström et al. (2004a) find a gradient of -0.099 kpc^{-1} in $[\text{Fe}/\text{H}]$ in main sequence stars from the Geneva Copenhagen Survey (Nordström et al. 2004b; Holmberg, Nordström & Andersen 2007). Daflon et al. (2009) report -0.04 kpc^{-1} in $[\text{S}/\text{H}]$ in OB stars. Frinchaboy et al. (2013) derive -0.09 kpc^{-1} in $[\text{M}/\text{H}]$ in open clusters. Hayden et al. (2014) also find -0.09 kpc^{-1} in $[\text{M}/\text{H}]$ for $R_{\text{gal}} \gtrsim 6 \text{ kpc}$ for low- α stars, but find the gradient to be relatively flat within $R_{\text{gal}} \lesssim 6 \text{ kpc}$. Weinberg et al. (2019) report a gradient of -0.06 kpc^{-1} in $\text{mode}([\text{Mg}/\text{H}])$ for upper red giant branch stars in the disc (see their Fig. 23). In tentative agreement with these studies, we adopt a slope of -0.08 kpc^{-1} . To set the normalization, we assume the $\text{mode}([\alpha/\text{H}])$ to be $\sim +0.3$ at $R_{\text{gal}} = 4 \text{ kpc}$, since this would produce $\text{mode}([\alpha/\text{H}]) \approx 0$ at $R_{\text{gal}} = 7 - 9 \text{ kpc}$. This results in the following form for η as a function of Galactocentric radius:

$$\eta(R_{\text{gal}}) = \frac{y_{\alpha}^{\text{CC}}}{Z_{\alpha, \odot}} 10^{(-0.08 \text{ kpc}^{-1})(R_{\text{gal}} - 4 \text{ kpc}) + 0.3} + r - 1 \quad (8)$$

where we adopt our CCSN yield of O for y_{α}^{CC} and the solar abundance of O of $Z_{\text{O}, \odot} = 0.00572$ based on Asplund et al. (2009). We plot this adopted scaling in the top panel of Fig. 3, highlighting a value of ~ 2.15 for the solar circle with a red dotted line. This does assume a uniformly linear gradient at all R_{gal} , in tension with the findings of Hayden et al. (2014) who find it to flatten within $\sim 6 \text{ kpc}$. However, this procedure can be easily repeated for any desired gradient, since the functional form simply goes into the power of 10 in equation (8).

Both AGB star enrichment and the recycling of previously produced metals in this paper proceed as they did in Johnson & Weinberg (2020), with the caveat that the mass is added to the annulus that a stellar population is in at a given time, which may or may not be the annulus it was born in. Recycling proceeds according to the Kalirai et al. (2008) initial-remnant mass relation assuming a Kroupa (2001) IMF and a mass-lifetime relationship of $\tau = 1.1\tau_{\odot}(M/M_{\odot})^{-3.5}$, where $\tau_{\odot} = 10 \text{ Gyr}$ is the main sequence lifetime of the sun and the factor of 1.1 accounts for the post-main sequence lifetime. VICE in its current version forces an AGB enrichment channel in all models; it is thus included in the present paper. For this enrichment channel, we adopt the net yields sampled on a table of stellar initial mass and metallicity from the FRUITY database (Cristallo et al. 2011). However, the AGB star yields of O and Fe are negligible compared to their supernova yields; we therefore conclude discussion of this component of our models here.

2.4 Star Formation Histories

VICE handles models in either infall, star formation, or gas mode, referring simply to which component of the evolutionary history the user has specified. The starburst models presented in Johnson & Weinberg (2020) ran in infall mode, but here we run VICE in star formation mode, because we are after specific forms for the star formation histories of our models. In Appendix A, we present justification of how we normalize the parameters of our star formation histories to produce a realistic model Galaxy at the present day. In short, it takes in a unitless description of the dependence of the SFH at a given Galactocentric radius, denoted $f(t|R_{\text{gal}})$, and a unitless

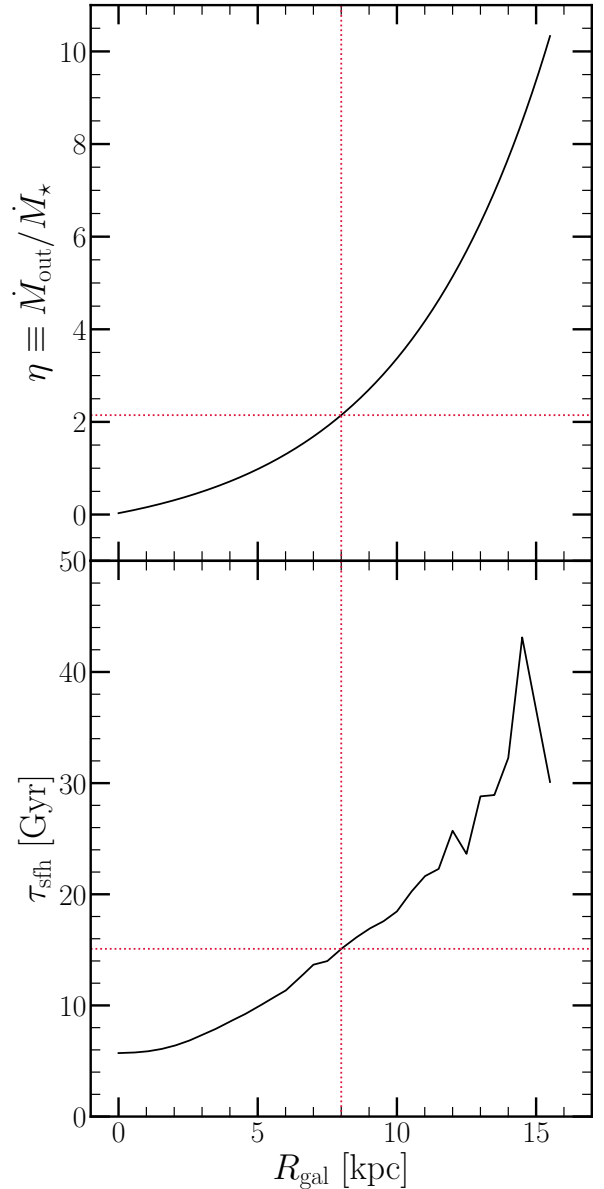


Figure 3. Top: Our implemented scaling of the mass loading factor η with Galactocentric radius (black) as defined by equation (8). **Bottom:** The e-folding timescales of the star formation histories of our model galaxies (black). These values come from a fit to the Σ_{\star} -age relation in bins of R/R_e for $10^{10.5} - 10^{11} M_{\odot}$ Sa/Sb Hubble type spiral galaxies as reported by Sánchez (2020, see discussion in § 2.4). The horizontal and vertical red dashed lines in both panels highlight a mass loading factor of $\eta \approx 2.15$ and a star formation timescale of $\tau_{\text{sfh}} \approx 15 \text{ Gyr}$ at an assumed radius of the sun of $R_{\odot} = 8 \text{ kpc}$.

description of the present day stellar surface density gradient, denoted $g(R_{\text{gal}})$. We integrate $f(t|R_{\text{gal}})$ with time for each annulus, assuming R_{gal} to correspond to the centre of the zone, and attach a prefactor to $f(t|R_{\text{gal}})$ in each annulus such that the desired gradient is achieved with a total stellar mass similar to the Milky Way. This procedure neglects the impact of radial migration, assuming that it does not significantly alter the form of $g(R_{\text{gal}})$. We demonstrate that these assumptions hold in §2.6, in which we also detail our adopted form of $g(R_{\text{gal}})$. As long as this assumption is not violated,

the equation derived in Appendix A can be used to calculate these prefactors for future models of Milky Way-like galaxies.

In the present paper, we present four fiducial SFHs, which we dub “constant”, “inside-out”, “late-burst”, and “outer-burst”. They’re defined as follows:

- **Constant:** The SFH at a given radius is time-independent.

$$f_C(t|R_{\text{gal}}) = 1 \quad (9)$$

This case is of particular theoretical interest because it quantifies the effect of stellar migration while removing the impact of a time-dependent SFH.

- **Inside-Out:** This is our fiducial SFH.

$$f_{\text{IO}}(t|R_{\text{gal}}) = (1 - e^{-t/\tau_{\text{rise}}})e^{-t/\tau_{\text{sff}}} \quad (10)$$

We adopt this mathematical form over a more traditional linear-times-exponential characterization, because the latter does not offer control over the position of the maximum SFR. The form we adopt has a maximum near τ_{rise} , for which we adopt a value of 2 Gyr everywhere here. This produces a peak in star formation at lookback times of ~ 10 Gyr, roughly corresponding to a redshift of $z \approx 2$, in agreement with observational results on the cosmic SFH (Madau & Dickinson 2014). In this paper, τ_{sff} is a function of R_{gal} , discussed in this section. We present results assuming this model throughout this paper except in cases where a different SFH impacts the predictions.

- **Late-Burst:** In this model, the inside-out SFH is modified to exhibit a recent, gradual burst in star formation described by a Gaussian:

$$f_{\text{LB}}(t|R_{\text{gal}}) = f_{\text{IO}}(t|R_{\text{gal}})(1 + A_b e^{-(t-t_b)^2/2\sigma_b^2}) \quad (11)$$

A_b is a dimensionless parameter describing the strength of the starburst, t_b is the time of the local maximum in the SFH during the burst, and σ_b is the width of the Gaussian describing it. This model being loosely motivated by the findings of Mor et al. (2019) and Isern (2019), we adopt $A_b = 1.5$, $t_b = 10.2$ Gyr, and $\sigma_b = 1$ Gyr, finding in practice that $A_b = 1.5$ produces a local maximum SFR that is a factor of ~ 2 larger than the preceding local minimum.

- **Outer-Burst:** A variation of the late-burst model in which only $R_{\text{gal}} \geq 6$ kpc experience the starburst. This is loosely motivated by the findings of Vincenzo & Kobayashi (2020) where a hydrodynamical simulation of a Milky Way-like galaxy showed radially dependent infall.

$$f_{\text{OB}}(t|R_{\text{gal}}) = \begin{cases} f_{\text{IO}}(t|R_{\text{gal}}) & (R_{\text{gal}} < 6 \text{ kpc}) \\ f_{\text{LB}}(t|R_{\text{gal}}) & (R_{\text{gal}} \geq 6 \text{ kpc}) \end{cases} \quad (12)$$

Although we do not consider such models here, an investigation into the impact of more episodic star formation histories would be an interesting extension of the present paper. For example, VICE has all of the necessary capabilities to handle models in which major episodes of star formation coincide with close passages of the Sagittarius dwarf (e.g. Ruiz-Lara et al. 2020).

We derive the scaling of the e-folding timescales of star formation τ_{sff} with R_{gal} from the data in Sánchez (2020). They present the stellar surface density Σ_\star as a function of age in bins of R/R_e for MaNGA galaxies, where R_e is the half-light radius. Here we take their $M_\star = 10^{10.5} - 10^{11} M_\odot$ bin for Sa/Sb spirals and simultaneously fit the normalization and e-folding timescale τ_{sff} of our $f_{\text{IO}}(t|R_{\text{gal}})$ form to the data. Although the normalization is irrelevant to our models and determined via the method outlined in Appendix A, we adopt the resulting $\tau_{\text{sff}} - R_{\text{gal}}$ relation in our models. With our adopted stellar surface density gradient (see discussion in §2.6), we know the present-day half-mass radius to be very near 4

kpc. The findings of García-Benito et al. (2017) and González Delgado et al. (2014) suggest that half-light radii are marginally larger than half-mass radii. Based on equation (4) of González Delgado et al. (2014) relating the two for circular apertures, we expect our model Galaxy to have a half-light radius near 5 kpc. We therefore adopt $R_e = 5$ kpc to convert the $\tau_{\text{sff}} - R_{\text{gal}}/R_e$ relation resulting from our fit to the Sánchez (2020) data into a $\tau_{\text{sff}} - R_{\text{gal}}$ relation. If there are references suggesting a similar value for the Milky Way, we should note them here.

We illustrate this relationship in the bottom panel of Fig. 3, noting that the resulting timescales are long, particularly for the outer Galaxy. With a red dotted line, we highlight a value of $\tau_{\text{sff}} \approx 15$ Gyr at an assumed orbital radius of the sun of $R_\odot = 8$ kpc. Although these timescales at most radii are considerably longer than a Hubble time, this is no cause for worry; this simply means that these regions of the Galaxy in our models experience less than 1 e-folding in their SFR, and that in the outer Galaxy the SFH is nearly constant after the initial rise in the first ~ 2 Gyr. It is nonetheless interesting that these timescales are considerably longer than that derived for the cosmic SFH (Madau & Dickinson 2014).

We plot the resultant SFHs of our models in the top row of Fig. 4 for a handful of radii. At all timesteps, the gas supply is known via the star formation efficiency timescale τ_\star (see discussion in §2.5). This quantity is illustrated in the bottom row of Fig. 4. VICE automatically calculates the implied infall rate by comparing the amount of gas lost to outflows and star formation in a given timestep to that which is required to sustain the user-specified level of star formation at the next timestep; we assume the infalling gas to be of zero metallicity at all times. This quantity is shown in the middle row of Fig. 4.

2.5 Star Formation Efficiency

The term “star formation efficiency” (SFE) is somewhat overloaded in the literature. In the star formation and feedback community, it usually refers to the fraction of a molecular cloud’s mass which will eventually be converted into stars. In the chemical evolution literature, however, it typically refers to the inverse timescale relating the SFR within some star forming reservoir and the mass of gas in that region: $\tau_\star \equiv \Sigma_g / \dot{\Sigma}_\star$. High (Low) values of τ_\star indicate slow (fast) star formation and thus low (high) SFE; when we refer to SFE here, we’re referring to the definition based on this timescale. In the star formation and feedback literature, this is often referred to as the “depletion time”.

Based on the findings of Kennicutt (1998), it is common practice in the chemical evolution literature a single power-law describing the relationship between the surface densities of gas and star formation Σ_g and $\dot{\Sigma}_\star$, often referred to as the star formation law or the Kennicutt-Schmidt relation:

$$\dot{\Sigma}_\star \sim \Sigma_g^N \quad (13)$$

Kennicutt (1998) derive $N = 1.4 \pm 0.15$ relating the total $\dot{\Sigma}_\star$ and Σ_g within the disc across a sample of quiescent spiral galaxies and infrared and circumnuclear starbursts. However, recent studies have found evidence that much of the observed scatter in this relation is physical in origin (de los Reyes & Kennicutt 2019) and that there are significant breaks in both the power-law index and zero-points (Kennicutt & de los Reyes 2020). Much of the uncertainty surrounding the details of the star formation law is a consequence of the ongoing debate about the CO-to-H₂ conversion factor (Kennicutt & Evans 2012; Liu, Gao & Greve 2015). Although Ellison et al. (2020a) demonstrate that there are significant galaxy-to-galaxy variations in the star formation law, suggesting that

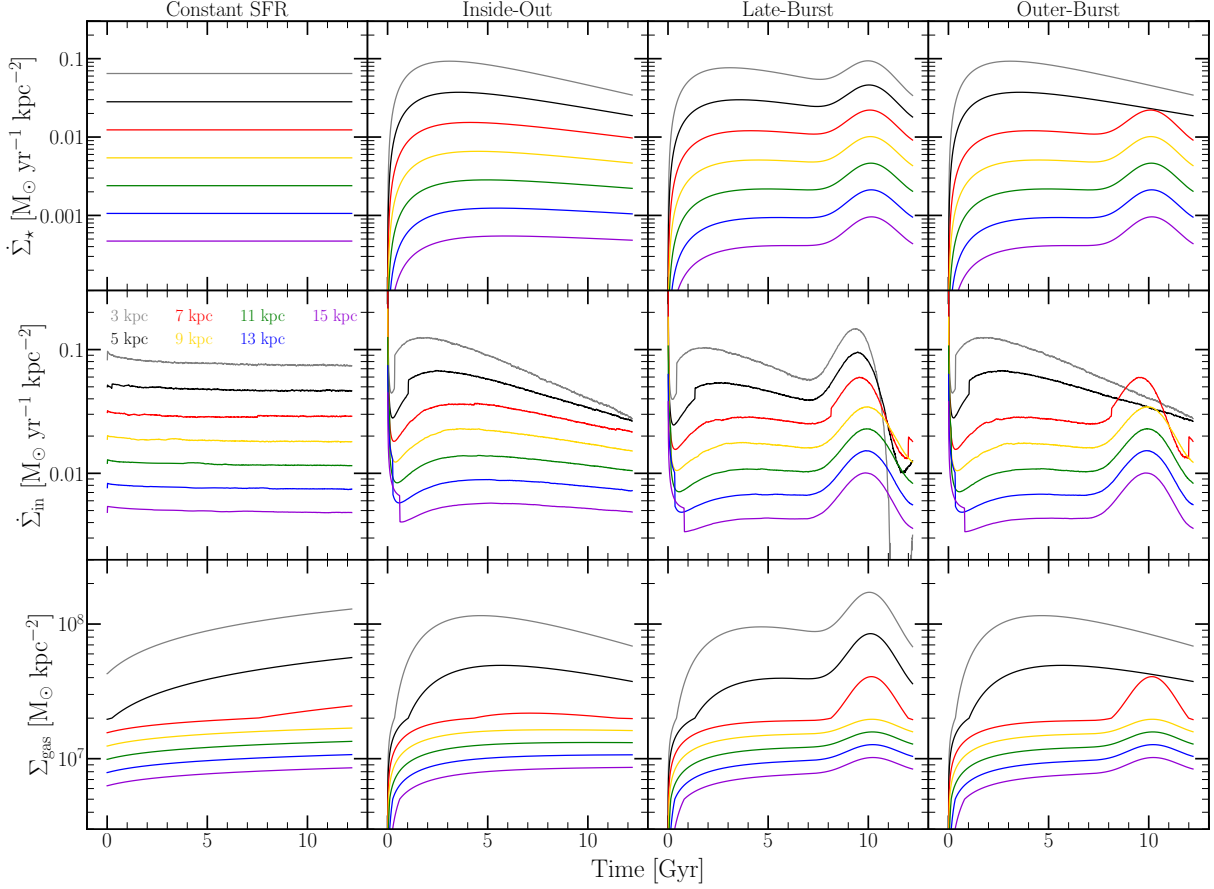


Figure 4. The surface densities of star formation $\dot{\Sigma}_\star$ (top row), infall $\dot{\Sigma}_{\text{in}}$ (middle row), and gas Σ_{g} (bottom row) as functions of simulation time for our four fiducial SFHs: constant (far left), inside-out (left middle), late-burst (right middle), and outer-burst (far right). We plot curves for the annuli whose inner radii are 3 kpc (grey), 5 kpc (black), 7 kpc (red), 9 kpc (yellow), 11 kpc (green), 13 kpc (blue), and 15 kpc (purple) (see equations (9), (10), (11), and (12) for the mathematical definition of each SFH).

individual galaxies do not follow the population averaged trend, [de los Reyes & Kennicutt \(2019\)](#) argue that this is still a reasonable recipe for Galaxy evolution models. We adopt such a formalism here.

[Krumholz et al. \(2018\)](#) compare model-predicted star formation laws to the observations of [Bigiel et al. \(2010\)](#) and [Leroy et al. \(2013\)](#) (see their Fig. 2). We find that the following by-eye fit to the power-law index N is a reasonable description of the aggregate data:

$$N = \begin{cases} 1.0 & (\Sigma_{\text{g}} \geq \Sigma_{\text{g},2}) \\ 3.6 & (\Sigma_{\text{g},1} \leq \Sigma_{\text{g}} \leq \Sigma_{\text{g},2}) \\ 1.7 & (\Sigma_{\text{g}} \leq \Sigma_{\text{g},1}) \end{cases} \quad (14)$$

where $\Sigma_{\text{g},1} = 5 \times 10^6 M_\odot \text{ kpc}^{-2}$ and $\Sigma_{\text{g},2} = 2 \times 10^7 M_\odot \text{ kpc}^{-2}$. The apparent linearity of the relationship above $\sim 2 \times 10^7 M_\odot \text{ kpc}^{-2}$ suggests that in this regime, star formation proceeds at the fastest possible rate, and that $\tau_\star \equiv \Sigma_{\text{g}}/\dot{\Sigma}_\star$ is constant. The observations of [Leroy et al. \(2013\)](#) and [Kennicutt & de los Reyes \(2020\)](#) would suggest that these are the surface densities at which the molecular fraction $f_{\text{mol}} = M_{\text{H}_2}/(M_{\text{H}_2} + M_{\text{HI}}) \approx 1$. We therefore adopt the assumption that above $\Sigma_{\text{g}} = 2 \times 10^7 M_\odot \text{ kpc}^{-2}$, τ_\star reaches its minimum value, and increases with decreasing f_{mol} . We denote this value as τ_{mol} , the value of τ_\star for a gas reservoir with $f_{\text{mol}} = 1$. This,

combined with our three-component power-law index N results in the following final form for our adopted star formation law:

$$\dot{\Sigma}_\star = \begin{cases} \Sigma_{\text{g}} \tau_{\text{mol}}^{-1} & (\Sigma_{\text{g}} \geq \Sigma_{\text{g},2}) \\ \Sigma_{\text{g}} \tau_{\text{mol}}^{-1} \left(\frac{\Sigma_{\text{g}}}{\Sigma_{\text{g},2}} \right)^{2.6} & (\Sigma_{\text{g},1} \leq \Sigma_{\text{g}} \leq \Sigma_{\text{g},2}) \\ \Sigma_{\text{g}} \tau_{\text{mol}}^{-1} \left(\frac{\Sigma_{\text{g},1}}{\Sigma_{\text{g},2}} \right)^{2.6} \left(\frac{\Sigma_{\text{g}}}{\Sigma_{\text{g},1}} \right)^{0.7} & (\Sigma_{\text{g}} \leq \Sigma_{\text{g},1}) \end{cases} \quad (15)$$

where we choose the power-law indices such that this formalism is consistent with equation (14), and prefactors are added to ensure piece-wise continuity. In implementation, VICE requires the $\tau_\star - \dot{\Sigma}_\star$ relation when ran in star formation mode and the $\tau_\star - \Sigma_{\text{g}}$ relation when ran in infall and gas modes. Both follow algebraically from this relationship given the substitution $\tau_\star \equiv \Sigma_{\text{g}}/\dot{\Sigma}_\star$.

Although it is more physically motivated to use an adopted star formation law to infer a star formation rate from the ISM properties at a given timestep, as discussed in § 2.4, we are using VICE in star formation mode. This means that it is $\dot{\Sigma}_\star$ which is specified *a priori* by our models - not Σ_{g} . That is, VICE is inferring Σ_{g} from $\dot{\Sigma}_\star$ in our models, not the other way around. While we acknowledge the findings of [Ellison et al. \(2020b\)](#), this another reason we must invoke a simple parameterization for the star formation law, which [Kennicutt & de los Reyes \(2020\)](#) argue is still a reasonable approach. This decision also means that changing our assumptions about the

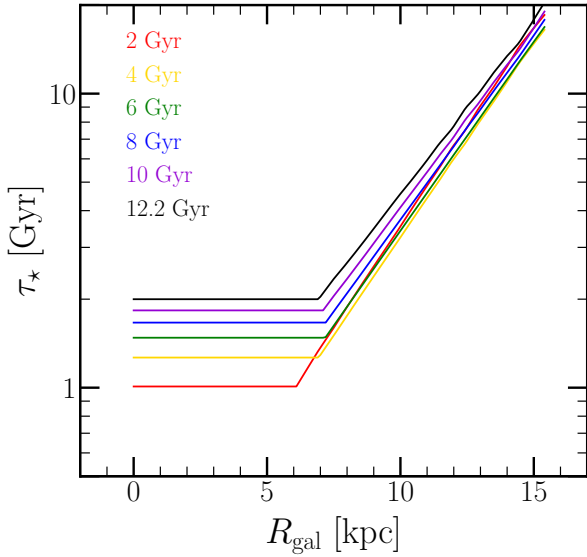


Figure 5. The star formation efficiency timescale τ_\star as a function of Galactocentric radius at simulation times of 2 Gyr (red), 4 Gyr (yellow), 6 Gyr (green), 8 Gyr (blue), 10 Gyr (purple), and 12.2 Gyr (the present day, black) predicted by our inside-out SFH model.

star formation law do not impact our SFHs, instead impacting the inferred Σ_g as a function of radius and time.

Based on the observed Kennicutt-Schmidt at different redshifts, [Tacconi et al. \(2018\)](#) suggest that τ_{mol} should scale with redshift z and the deviation from the star forming main sequence δMS via $\tau_{\text{mol}} \propto (1+z)^{-0.6} \delta\text{MS}^{-0.44}$. We don't take into account the effect of δMS in our models, but we do investigate the redshift dependence. A reasonable approximation to the $t-z$ relation out to $z \approx 3$ assuming typical ΛCDM cosmology is given by:

$$\frac{t}{t_0} \approx (1+z)^{-5/4} \quad (16)$$

where t_0 is the present-day age of the universe, and t is not simulation time but the age of the universe. Plugging this relation into the [Tacconi et al. \(2018\)](#) scaling yields the following time-dependence for τ_{mol} :

$$\tau_{\text{mol}} = \tau_{\text{mol},0} (t/t_0)^{12/25} \approx \tau_{\text{mol},0} (t/t_0)^{1/2} \quad (17)$$

where $\tau_{\text{mol},0}$ is simply τ_{mol} at the present day. We generalize this formula to the following form:

$$\tau_{\text{mol}} = \tau_{\text{mol},0} (t/t_0)^\gamma \quad (18)$$

In this paper we present models which adopt $\tau_{\text{mol},0} = 2$ Gyr ([Leroy et al. 2008, 2013; Tacconi et al. 2018](#)) and $\gamma = 1/2$ based on this argument. We have also ran simulations which adopt $\tau_{\text{mol},0} = 1$ Gyr and $\gamma = 0$ (a time-independent τ_{mol}), and found similar results. In all timesteps an annuli, VICE infers Σ_g from $\dot{\Sigma}_\star$ given our equations (15) and (18).

In Fig. 5, we plot τ_\star as a function of R_{gal} at six different time stamps predicted by our fiducial, inside-out SFH model. At $R_{\text{gal}} \lesssim 6$ kpc, τ_\star is near τ_{mol} at all times, implying a molecular fraction of unity at these radii. Although this prediction is likely unrealistic because 21-cm line observations suggest the presence of neutral hydrogen as close to the Galactic centre as several hundred pc ([Kalberla & Kerp 2009](#)), we find in practice that changing our

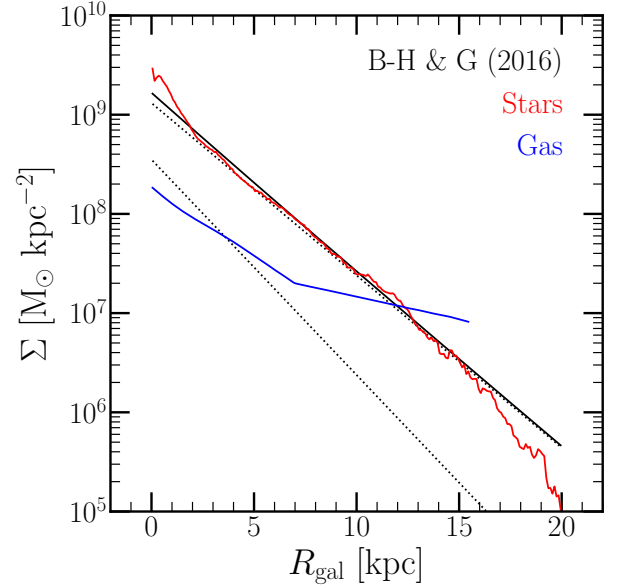


Figure 6. The surface density of gas (blue) and stars (red) as predicted by our inside-out SFH model. The dotted black line with the higher normalization denotes a thin disc profile with scale length $R_t = 2.5$ kpc; the other denotes a thick disc profile with scale length $R_T = 2.0$ kpc, and a ratio of $\Sigma_T/\Sigma_t = 0.27$ at $R_{\text{gal}} = 0$. The solid black line denotes the sum of the two; this is the surface density gradient of the Milky Way as reported by [Bland-Hawthorn & Gerhard \(2016\)](#), renormalized to imply the same total stellar mass within the disc as our models.

assumptions about the star formation law does not impact our conclusions. In collecting results for this paper, we investigated purely linear, purely power-law, and broken power-law characterizations, finding similar predictions in all cases. In general we find that the detailed form of the SFH, and to some extent the time-dependence of radial migration, exert much greater power in establishing the model predictions than does the star formation law. Nonetheless it is an interesting result that a $\dot{\Sigma}_\star - \Sigma_g$ relation informed by the observed, population averaged trend and the normalization of our SFHs implied by the stellar mass of the Milky Way predicts such a discrepancy with the observed HI distribution. We refrain from further discussion of this with the finding that it doesn't impact the conclusions detailed in the present paper.

2.6 Surface Density Gradient

As discussed in § 2.4, Appendix A presents justification of a recipe in which we select a unitless function describing the stellar surface density gradient $g(R_{\text{gal}})$. In setting the normalization, our model ensures that the integral of $g(R_{\text{gal}})$ over the surface area of the disc predicts a total stellar mass in agreement with that observed for the Milky Way. For this value, we adopt $M_\star^{\text{MW}} = (6.08 \pm 1.14) \times 10^{10} M_\odot$ ([Licquia & Newman 2015](#)). This is the total stellar mass of the Galaxy, including the bulge; [Licquia & Newman \(2015\)](#) report $(5.17 \pm 1.11) \times 10^{10} M_\odot$ as the mass of the disc alone. Although we aren't modeling the bulge here, our model extends to $R_{\text{gal}} = 0$ and our sample of candidate analog star particles from h277 includes those with bulge-like kinematics.

In this paper we adopt the following double exponential form for $g(R_{\text{gal}})$, describing the thin and thick disc components of the

Galaxy:

$$g(R_{\text{gal}}) = e^{-R_{\text{gal}}/R_t} + \frac{\Sigma_T}{\Sigma_t} e^{-R_{\text{gal}}/R_T} \quad (19)$$

where R_t and R_T are the scale radii of the thin and thick discs, respectively, and Σ_T/Σ_t is the ratio of their surface densities at $R_{\text{gal}} = 0$. We adopt $R_t = 2.5$ kpc, $R_T = 2.0$ kpc, and $\Sigma_T/\Sigma_t = 0.27$ based on the findings of [Bland-Hawthorn & Gerhard \(2016\)](#). We plot the single exponential forms of each disc component as a dotted black line in Fig. 6, with the solid black line denoting the sum of the two. Although these scale radii are smaller than the commonly adopted scale radius for a single exponential disc of $r_s \approx 3$ kpc (e.g. [Binney & Tremaine 2008](#)), our choice of a double exponential disc here necessitates a choice be made for not one but two scale radii.

We plot the resultant surface density gradients from our fiducial, inside-out SFH model in Fig. 6 as well, with red denoting the stellar gradient and the gas in blue. We note that the stellar gradient very nearly follows our target gradient denoted by the solid black line and expressed by equation (19). Stellar migration has indeed not altered the overall form of the gradient, simply introducing scatter around the adopted trend. Although there are slight enhancements at small R_{gal} and deficits at large R_{gal} , the agreement is excellent in the regions of the Galaxy where the gradient is best constrained observationally. The $R_{\text{gal}} > 15.5$ kpc populations are also composed entirely of stars that migrated there, since that is the radius at which we shut off star formation; with this mind, the under-prediction at these radii is unsurprising. Furthermore, in this paper we are interested primarily in the $R_{\text{gal}} = 3 - 15$ kpc range anyway, since this is the region where disc stars are the dominant populations. We also note that the gas gradient shows a break in the scale radius near $R_{\text{gal}} \approx 6$ kpc. This is a consequence of our adopted star formation law; at $\Sigma_g = 2 \times 10^7 \text{ M}_\odot \text{ kpc}^{-2}$ the relation changes from linear at higher densities to $\dot{\Sigma}_\star \sim \Sigma_g^{3.6}$ at lower densities (see discussion in § 2.5). Because we are running VICE in star formation mode, it's more accurate to say that Σ_g is a weak function of $\dot{\Sigma}_\star$ at $\Sigma_g \leq 2 \times 10^7 \text{ M}_\odot \text{ kpc}^{-2}$ in this range as opposed to $\dot{\Sigma}_\star$ being a strong function of Σ_g . When looking at the present-day gradient, this presents as a flattening of the gradient at the radius where $\Sigma_g = 2 \times 10^7 \text{ M}_\odot \text{ kpc}^{-2}$; further inspection along the y-axis of Fig. 6 confirms that this break indeed occurs at this value of Σ_g .

Although we adopt the [Licquia & Newman \(2015\)](#) stellar mass of the Milky Way here, we find similar results when taking a value which differs by an order of magnitude. While mass typically cancels in one-zone models of chemical evolution, the abundances instead determined by the evolutionary parameters (e.g. η and τ_\star), this value sets the normalization of the SFH $\dot{\Sigma}_\star(t, R_{\text{gal}})$ in our models. In turn this impacts the surface densities of gas Σ_g inferred at each timestep, and thus the abundances to some extent. This choice only matters insofar as the choice of star formation law matters, which we find to not impact our conclusions.

2.7 Summary

In summary, our fiducial model has an inside-out SFH with e-folding timescales derived from the observations of [Sánchez \(2020\)](#), see discussion in § 2.4. Radial migration proceeds in a manner in which our model stellar populations have a change in radius ΔR_{gal} informed from the h277 hydrodynamical simulation ([Christensen et al. 2012](#); [Zolotov et al. 2012](#); [Loebman et al. 2012, 2014](#); [Brooks & Zolotov 2014](#), see discussion in § 2.1). In the base-line model, stars move to their final radius with a $\sqrt{\text{age}}$ dependence ([Frankel et al. 2018, 2020](#) model stellar migration with a similar characterization; see

discussion in § 2.2). Using VICE to calculate abundances for O and Fe in this paper, our supernova yields are adopted from [Johnson & Weinberg \(2020\)](#), who in turn take these values from [Weinberg et al. \(2017\)](#). Outflows are characterized such that the equilibrium abundance of oxygen under a constant SFH follows an abundance gradient in agreement with observational results in the Milky Way (see discussion in § 2.3; [Nidever et al. \(2014\)](#) make use of similar methodology). Our star formation law is based on the [Bigiel et al. \(2010\)](#) and [Leroy et al. \(2013\)](#) data presented in comparison with theoretical models in [Krumholz et al. \(2018\)](#), see discussion in § 2.5). To describe the stellar surface density gradient, we adopt the two-exponential form describing the thin and thick discs from [Bland-Hawthorn & Gerhard \(2016\)](#), see discussion in § 2.6).

Our quality cuts imposed on the star particles from h277 yields a sample of 3,000,556 candidate analog star particles (see discussion in § 2.1), only $\sim 57\%$ of which have disc-like kinematics at the present day. Since we're modeling the thin and thick disc populations here, ~ 1.71 million is a much better estimate of the number of star particles that we can realistically sample from. We take $\Delta R_{\text{gal}} = 100$ pc as the width of each annulus from $R_{\text{gal}} = 0$ to 20 kpc and a timestep size of $\Delta T = 10$ Myr from $T = 0$ to 12.2 Gyr. With the resulting 200 zones and 1,221 timesteps, we let VICE form $n = 9$ stellar populations per annulus per timestep, resulting in 2,197,000 total stellar populations with predicted masses and abundances. While this is more than the number of disc particles in our sample of candidate analogs, we force the star formation rate to zero beyond $R_{\text{gal}} = 15.5$ kpc; while these stellar populations exist within VICE and are a part of the computational overhead, they have zero mass and thus do not contribute to the chemical evolution in our models. This results in 1,692,306 stellar populations with *non-zero* masses and abundances predicted by VICE, reasonably within the limit of what we can sample. These simulations run in ~ 2.5 hours and take up ~ 235 MB of disc space per output, including the extra data that we record for each stellar population's analog star particle. Lastly, we adopt a [Kroupa \(2001\)](#) IMF throughout this paper.

We have ran VICE for all four of our SFHs, all four migration models, and all four variations in τ_{mol} noted in § 2.5 - a total of 64 simulations, as well as a variety of other test cases. In this paper, we present results wherever the model prescriptions are sensitive to the assumptions. However, in general the differences can be understood with only the variations in star formation history and the qualitative notion that many stars have moved beyond their birth radius. VICE calculates abundances for nearly 2 million stellar populations per model; to ensure that resolution does not impact our conclusions, we have also ran variations with $n = 2$ stellar populations per zone per timestep, and found similar results in all cases.

3 COMPARISON TO OBSERVATIONS

We begin the comparison of our model predictions to observational data with the distribution of stellar populations in the [O/Fe]-[Fe/H] plane. We separate stars into bins based on their present-day Galactic regions defined by five bins in R_{gal} (3 - 5, 5 - 7, 7 - 9, 9 - 11, and 11 - 13 kpc) and three bins in $|z|$ (0 - 0.5, 0.5 - 1, and 1 - 2 kpc). Within each of the resulting 15 regions, we sample 10,000 stars at random from our base-line inside-out SFH model. Since stars in VICE are stand-ins for entire stellar populations, we let the probability of sampling one of them be proportional to its present day mass. We plot the results of this procedure in Fig. 7, colour-coding each stellar population by its birth radius; for reference, we also plot the gas-

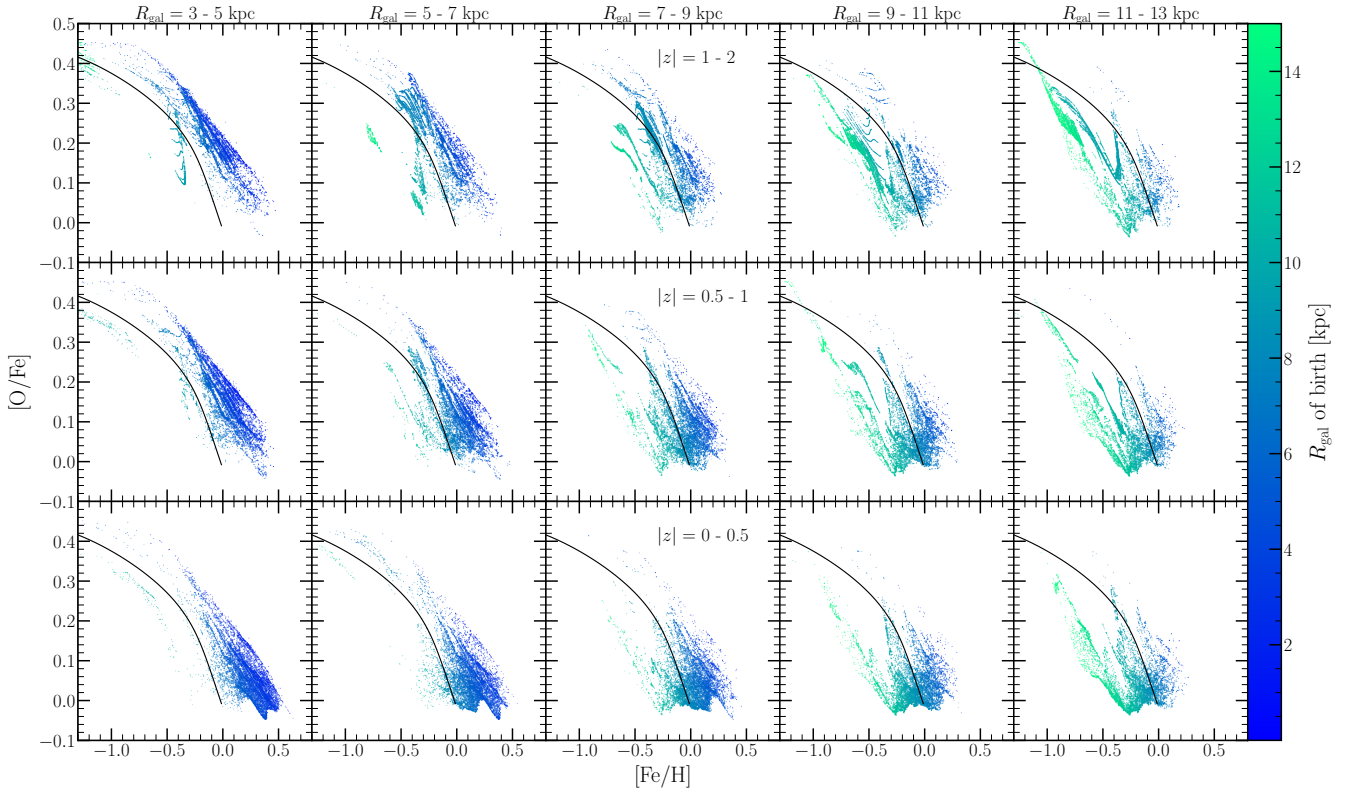


Figure 7. $[\text{O}/\text{Fe}]-[\text{Fe}/\text{H}]$ diagrams for 15 Galactic regions spanning five bins in R_{gal} and $|z|$. Each region has its own panel, with radial bins shown in columns denoted at the top, and with bins in $|z|$ shown in rows denoted in text in the middle column. For each region, we plot $N = 10,000$ points sampled from our simulated stellar populations predicted by our inside-out SFH model, where the probability of sampling is proportional to the present-day mass of each stellar population. In all panels, points are colour-coded according to the Galactocentric radius of birth of the stellar population. For reference, we plot in a solid black line in all panels the gas-phase $[\text{O}/\text{Fe}]-[\text{Fe}/\text{H}]$ track predicted by the same SFH in the $R_{\text{gal}} = 8$ kpc annulus, but with the post-processing migration model; this curve is the same in all panels.

phase track which resulted from the $R_{\text{gal}} = 8$ kpc annulus with the post-processing migration model in a black solid line in all panels.

In Fig. 7, we note that high- α sequence stars are predicted to be the dominant population at small R_{gal} and high $|z|$; conversely, the low- α sequence dominates the statistics at large R_{gal} and low $|z|$. This is consistent with the observational results of Hayden et al. (2015), who present a density map in the $[\text{O}/\text{Fe}]-[\text{Fe}/\text{H}]$ for the same Galactic regions (see their Fig. 4). Furthermore, the locus of the low- α sequence shifts from super-solar $[\text{Fe}/\text{H}]$ to sub-solar $[\text{Fe}/\text{H}]$ with increasing R_{gal} , a shift which is expected given the abundance gradient that we have built into our models (see discussion in § 2.3). The colour-coding of the points further suggests that the width of the low- α sequence arises out of stellar migration. Though this wouldn't occur in our models without mixing, it is to some extent expected from that in combination with the built-in gradient. Nonetheless this theoretical interpretation of the low- α sequence is consistent with the arguments of Schönrich & Binney (2009) and Nidever et al. (2014).

We clarify that we do not claim to recover the bimodality in $[\alpha/\text{Fe}]$ as observed here. Although there are authors who argue to have successfully reproduced such results using an inside-out SFH with stellar migration (e.g. Sharma et al. 2020), we find that our fiducial model fails to reproduce these results (see discussion in § 3.3). These results do nonetheless suggest that the spatial dependence of the two sequences can be attributed to stellar migration. Lastly,

we note that we find similar results with our other three SFHs, increasing confidence in our argument that migration establishes such a spatial dependence rather than the SFH. The only notable difference is that the starburst models predict a slightly higher characteristic $[\text{O}/\text{Fe}]$ for the low- α sequence ($\sim +0.1$). This is a natural consequence of the starburst producing young, α -enhanced stars in excess of what is predicted by the baseline model (Johnson & Weinberg 2020).

3.1 Abundance Gradients

We continue by assessing the impact of stellar migration on the gas-phase tracks in the $[\text{O}/\text{Fe}]-[\text{Fe}/\text{H}]$ plane. To this end, we compare the predictions of our post-processing migration model, which has stars stay at their radii of birth until they instantaneously migrate at the present day, and our diffusion model, which has stars migrating continuously with a \sqrt{age} dependence. In the left-hand panel of Fig. 8, we plot the $[\text{O}/\text{Fe}]-[\text{Fe}/\text{H}]$ tracks at several radii assuming the inside-out SFH, with post-processing shown in dotted lines and the diffusion in solid lines. We also mark simulation times of 2, 4, 6, 8, 10, and 12.2 Gyr on each track for reference.

We note first and foremost that there are considerable differences between the two sets of tracks, particularly at high $[\text{O}/\text{Fe}]$. We demonstrate here that this arises out of variability in SN Ia rates caused by the time-dependent radial migration of the diffusion

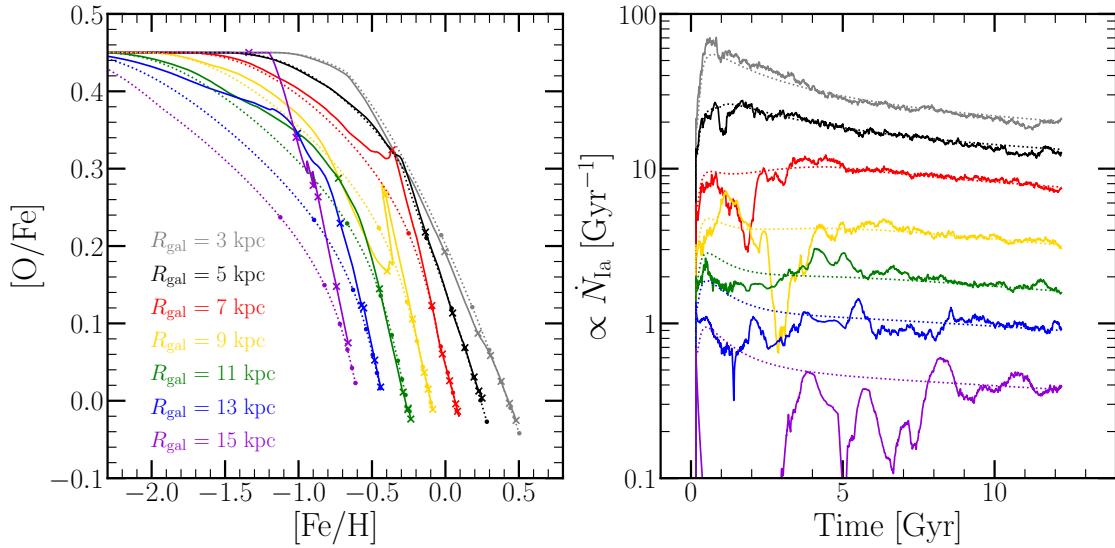


Figure 8. *Left:* Gas phase evolutionary tracks in the $[O/Fe]$ - $[Fe/H]$ plane for our inside-out SFH with either post-processing (dotted lines) or diffusion (solid lines) migration models. We plot tracks for seven annuli, colour-coded according to their Galactocentric radius and denoted by the legend in the lower-left. We mark simulation times of 2, 4, 6, 8, 10, and 12.2 Gyr in X's for the diffusion model and points for the post-processing model. *Right:* As a function of simulation time, a proxy for the SN Ia rate using the total time-derivative of the Fe mass in a given annulus, calculated by subtracting the contribution from recycling and CCSN enrichment and adding back that lost to star formation and outflows. We show these rates for the same annuli as in the left-hand panel, multiplying them by various prefactors to improve clarity.

model. From our VICE outputs, the total time derivative of the Fe mass in a given annulus can be obtained by its change across a single timestep. By then subtracting the CCSN contribution (known exactly given our adopted yield and the SFR), approximately correcting for recycling, and adding back that which was lost to star formation and outflows, we obtain a simple estimate of the rate of Fe production by SNe Ia.

We plot this proxy as a function of simulation time in the right-hand panel of Fig. 8, with dotted and solid lines again denoting post-processing and diffusion migration models and the same colour-coding as in the left-hand panel; we have also multiplied these curves by various prefactors to improve clarity. As expected, the post-processing model predicts a SN Ia rate which is a smooth function of time at a given R_{gal} . The diffusion model on the other hand exhibits significant variability on \sim Gyr timescales; the time-averaged SN Ia rate tends to follow the post-processing prediction, but the instantaneous rates do not agree. A close comparison allows one to realize that whenever one of the tracks in the left-hand panel shows higher (lower) $[O/Fe]$ at a given $[Fe/H]$, there is an excess (deficit) in the SN Ia rate at a similar time and radius. Early times in the $R_{gal} = 15$ kpc annulus illustrates a rather extreme example whereby the SN Ia rate is effectively zero for nearly 3 Gyr. We also note that the fractional amplitude of the variability increases with R_{gal} ; the log-scaled y-axis makes this clear. This makes sense physically because the lower stellar number density in the outer Galaxy means it would be much more susceptible to sampling noise. That is, a single star migrating has a larger fractional impact at large radii than small radii.

Although one may expect the rates predicted by the two migration models to agree based on the dynamical argument that a star migrating outward should be balanced by a star migrating inward due to the conservation of energy, the SN Ia rate depends not only on stellar number density but also on the masses and ages of the stellar populations. While an inwardly migrating star should be bal-

anced dynamically by an outwardly migrating one, the SN Ia rate is unaffected only when the two have masses and ages such that the SN Ia DTD has the same value for both stars. Fluctuations in the SN Ia rate at these amplitudes can be understood through a comparison of the timescales associated with radial migration and SN Ia events. In Fig. 1, we plotted the distribution of final radii in bins of birth radius and age, which are used in driving stellar migration in our models (see discussion in §2.1). From this, we noted that $\sim 40\%$ of h277 star particles migrated beyond their birth radius by the time they were ~ 2 Gyr old. Though our adopted form differs slightly in detail, if the SN Ia DTD is a $\sim t^{-1}$ power-law with a minimum delay time of ~ 100 Myr (Maoz & Mannucci 2012; Maoz & Graur 2017), then there should be similar numbers of SN Ia events with delay times between 1 and 10 Gyr as there are between 100 Myr and 1 Gyr. While our $R_{gal} = 15$ kpc annulus is something of an extreme example, when one realizes that this means \sim half of SN Ia progenitors may move significantly beyond their birth radius, the amplitude of the variability seen in the right-hand panel of Fig. 8 is not surprising. The fact that $>10\%$ of events are seen at >10 kpc from their host galaxies in the ASAS-SN bright SN catalog (Holoien et al. 2019) adds qualitative, observational support to the argument that SN Ia progenitors may often form at significantly different radii than where the explosions are observed.

We thus argue that the radial migration of nucleosynthetic yields can occur alongside stellar migration for delayed sources. Though we do not investigate this effect for such elements in this paper, it would be reasonable to expect similar predictions for s-process elements produced in AGB stars like carbon, nitrogen, strontium, yttrium, and zirconium as well as r-process elements from neutron star mergers if the associated DTD is sufficiently long. What we really learn from this investigation is that tracks are not simple functions when stellar migration is taken into account. To first order, they're characterized by the late-time equilibrium abundance and the value of τ_{\star} setting the position of the “knee” (Weinberg et al.

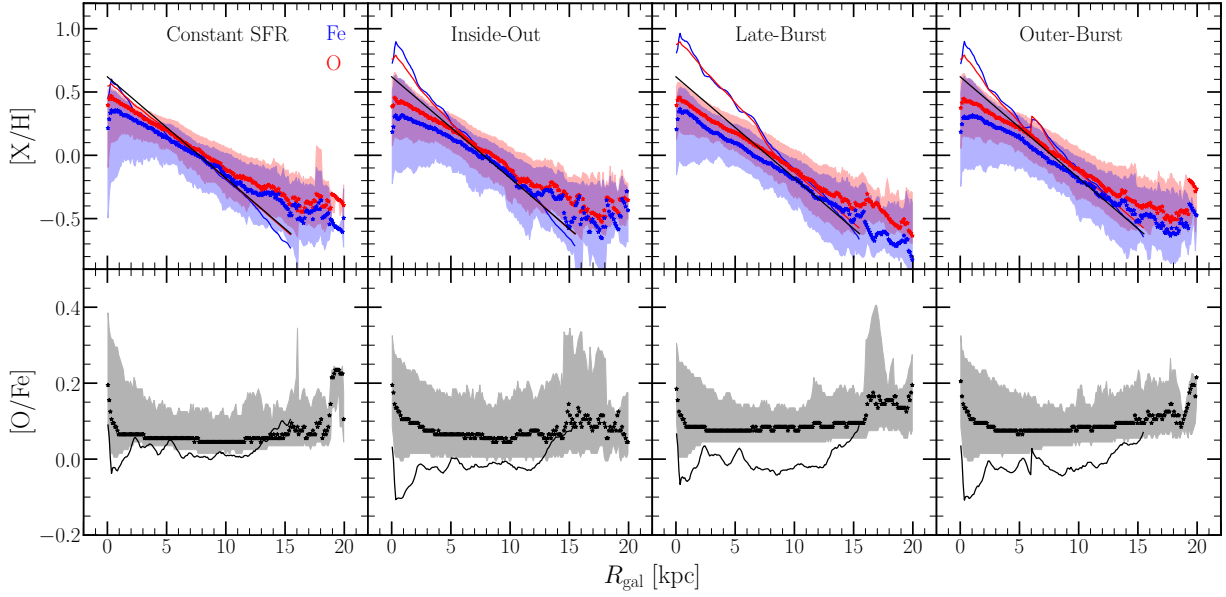


Figure 9. Radial abundance gradients in [O/H] (top, red), [Fe/H] (top, blue), and [O/Fe] (bottom) for our four fiducial SFHs - constant (far left), inside-out (left-middle), late-burst (right-middle), and outer-burst (far right). We plot the gas-phase abundance at the present day as a function of Galactocentric radius in solid lines. Stars denote the median of the stellar MDF of the 100-pc width annulus at a given radius, with shaded regions marking the 16th and 84th percentiles thereof. Black lines in the top panels denote our target $[\alpha/H]$ gradient of $\text{mode}([\alpha/H]) = +0.3$ at $R_{\text{gal}} = 4$ kpc with a slope of -0.08 kpc^{-1} .

2017), though migration causes noticeable variations which should depend on the details of the adopted dynamical history. In § 3.4, we demonstrate that this is a means with which truly young, super-solar $[\alpha/\text{Fe}]$ stars in the solar neighborhood can be explained theoretically.

We continue with an investigation into the radial abundance gradients predicted by our models. To some extent, a gradient is built into our models via a scaling of the mass loading factor η with Galactocentric radius (see discussion in § 2.3). In parameterizing the $\eta - R_{\text{gal}}$ scaling, we assumed our constant SFH model and the associated equilibrium abundance for alpha elements. Like the surface density gradient, we also assumed that stellar migration does not alter the overall form. We plot the radial [O/H] and [Fe/H] gradients predicted by all our models in the top row of Fig. 9, and the [O/Fe] gradients in the bottom row. In all panels, stars denote the median abundance in each annulus, and the shaded region denotes the 16th and 84th percentiles of the MDF in that zone; solid lines denote the gas-phase gradient at the present day. Although we built the gradient into our models based on the mode abundance, we illustrate them here according to the median; we find that with annuli as narrow as $\Delta R_{\text{gal}} = 100$ pc, the mode is a sufficiently noisy statistic to introduce noticeably more scatter in this relation. Nonetheless we have verified that it follows the trend implied by our target gradient, illustrated by the solid black line. The median gradient for all of our model SFHs follows a slightly shallower trend than the mode, which is expected when the metallicity distribution is skew-negative in the inner Galaxy and skew-positive in the outer Galaxy.

We note that our models indeed recover an $R_{\text{gal}}\text{--}[\text{O}/\text{H}]$ relation resembling that which was adopted. As was the case for the surface density gradient (see discussion in § 2.6), stellar migration appears to only introduce scatter. While our procedure for setting the abundance gradient did not consider Fe, our models predict it to follow a gradient similar to that of O. We further note that all SFHs predict an [O/Fe] gradient which is relatively flat at all radii,

steepening only at very small and very large R_{gal} . The trend toward higher [O/Fe] beyond $R_{\text{gal}} = 15.5$ kpc is expected, since this is the radius at which we shut off star formation; all stellar populations at these radii at the present day formed in the disc and migrated there, meaning this region of space in our model is populated only by stars sufficiently old to have migrated such distances. Because they're old, they also tend to be α -enhanced. This is consistent with the findings of Radburn-Smith et al. (2012), who argue that the outskirts of the NGC 7793 disc formed largely out of stellar migration. **Observational reference on the increase in [O/Fe] at small R_{gal} ? Maybe Hayden et al. (2015), but I'm not sure.**

We also note that our models predict differences between the stellar and present-day gas-phase gradients which are sensitive to the adopted SFH. In the constant SFH model, the gas-phase gradient follows the mode abundance by construction. In the inside-out, late-burst, and outer-burst models, the ISM at small R_{gal} is considerably more metal-rich than the stars at similar radii. The late-burst model shows the largest difference; this is a consequence of the starburst at small R_{gal} , an effect which is absent in the outerburst model. In accretion-induced starbursts, re-enrichment can briefly produce super-equilibrium abundances in the gas-phase which then decay back to the equilibrium abundance as the SFR declines (Johnson & Weinberg 2020). This effect can also be seen in the outer-burst model; at R_{gal} slightly larger than 6 kpc where the starburst did occur, the abundances are larger than at slightly less than 6 kpc, where the star burst did *not* occur. Altogether, these differences are reflective of the notion that the stellar abundance gradient is sensitive to stars of all ages and thus the entire star formation history, while the gas-phase gradient is more reflective of enrichment over the previous depletion time.

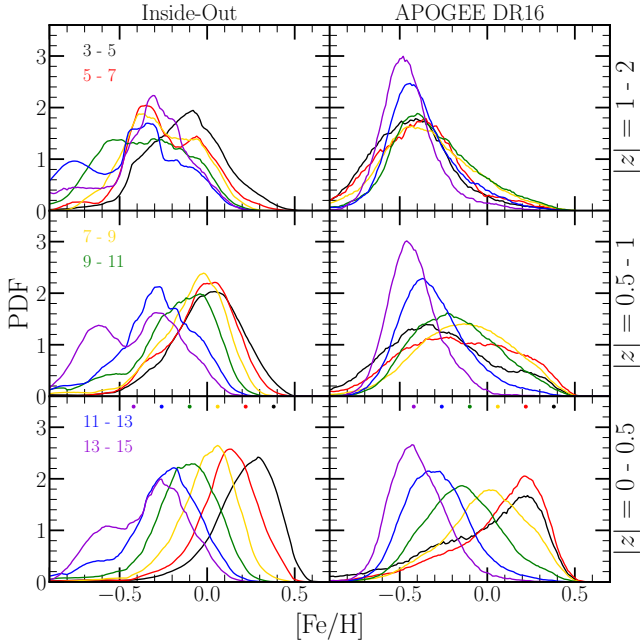


Figure 10. Metallicity distribution functions (MDFs) in $[\text{Fe}/\text{H}]$ predicted by our fiducial, inside-out model (left) and as observed in APOGEE DR16 (right), for stars and simulated stellar populations with present-day $|z| = 0 - 0.5$ kpc (bottom), $0.5 - 1$ kpc (middle), and $1 - 2$ kpc (top). MDFs are shown in bins of Galactocentric radius: 3 - 5 kpc (black), 5 - 7 kpc (red), 7 - 9 kpc (yellow), 9 - 11 kpc (green), 11 - 13 kpc (blue), and 13 - 15 kpc (purple). The points near the top of the bottom panels denote what the mode abundance would be if it followed our target gradient of $[\text{Fe}/\text{H}] = +0.3$ at $R_{\text{gal}} = 4$ kpc with a slope of -0.08 kpc^{-1} exactly, assuming the inner radius of each bins (i.e. there is no point plotted for 15 kpc). All distributions are smoothed with a box-car width of $[\text{Fe}/\text{H}] \pm 0.1$ for clarity.

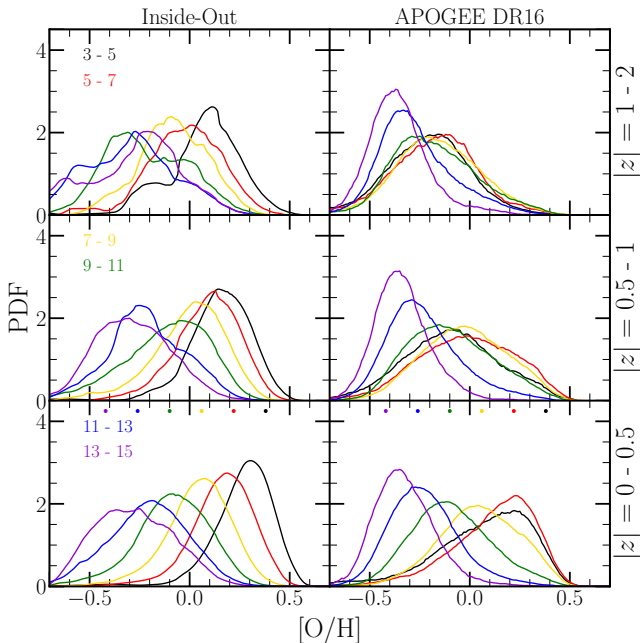


Figure 11. The same as Fig. 10, but for $[\text{O}/\text{H}]$.

3.2 Metallicity Distributions Functions

Metallicity distribution functions (MDFs) and how they vary with Galactic region are one of the core predictions of chemical evolution models. In this section, we compare our model predicted MDFs to those observed in the 16th data release of APOGEE (DR16; [Ahu-mada et al. 2020](#); [Majewski et al. 2017](#)). The data are reduced using the APOGEE Stellar Parameters and Chemical Abundances Pipeline (ASPCAP; [Holtzman et al. 2015](#); [García Pérez et al. 2016](#)). For further details of the APOGEE survey, a brief summary can be found in § 2 of [Weinberg et al. \(2019\)](#). We restrict our sample to stars with effective temperatures of $4000 \text{ K} \leq T_{\text{eff}} \leq 4600 \text{ K}$, surface gravities of $1.0 \leq \log g \leq 2.5$, and signal-to-noise ratios of at least 100. These cuts ensure that our sample consists of stars on the upper red giant branch, safely excluding red clump stars to avoid obvious systematics in the abundance distributions.

In the disc midplane, stars as observed by APOGEE are known to exhibit mode $[\alpha/\text{H}]$ and $[\text{Fe}/\text{H}]$ abundances that depend on Galactocentric radius, with a skew-negative distribution in the inner Galaxy and skew-positive in the outer Galaxy ([Hayden et al. 2015](#); [Weinberg et al. 2019](#)). Off the midplane, the MDFs converge on $[\alpha/\text{H}] \approx [\text{Fe}/\text{H}] \approx -0.5$. This result is replicated in the right-hand column of panels 10 and 11. The left-hand columns show the distributions predicted by our fiducial inside-out model. We note that these replicate the qualitative scaling of the mode $[\text{O}/\text{H}]$ and $[\text{Fe}/\text{H}]$ with present-day Galactocentric radius, though our APOGEE data suggest that the 3 - 5 and 5 - 7 kpc bins share a common mode abundance. This was also seen in [Hayden et al. \(2015\)](#). Our models do not predict this detail; this could indicate that we have incorrectly parameterized outflows in the inner Galaxy (see discussion regarding our scaling of the mass loading factor η with R_{gal} in § 2.3). We would expect a flat $[\text{X}/\text{H}]$ gradient and MDFs with similar modes if we simply chose it to be so by letting η be constant at small R_{gal} . Another possibility is the cessation of star formation in these regions; by tracing products of star formation such as HII regions ([Gustén & Mezger 1982](#)), supernova remnants ([Leahy & Wu 1989](#)), and pulsars ([Lyne, Manchester & Taylor 1985](#); [Case & Bhattacharya 1998](#)), the surface density of star formation $\dot{\Sigma}_{\star}$ in the Milky Way is known to reach a maximum at $R_{\text{gal}} \approx 4$ kpc (see Fig. 1 of [Peek 2009](#) and Fig. 2 of [Fraternali & Tomassetti 2012](#)). Our models by construction predict $\dot{\Sigma}_{\star}$ to decrease monotonically with R_{gal} (see Fig. 4). If the Milky Way has begun quenching star formation, a process which is believed to begin in the centres of galaxies at this mass (e.g. [Ellison et al. 2020b](#)), then fewer stars would form in the most metal-rich regions than do in our models, cutting off the MDF at high $[\text{O}/\text{H}]$ and $[\text{Fe}/\text{H}]$.

Beyond the midplane, our models fail to fully replicate the convergence of the MDFs at $[\text{X}/\text{H}] \approx -0.5$. The observed MDF at small radii shifts from skew-negative with a metal-rich mode to skew-positive with a metal-poor mode with increasing $|z|$. In our model predicted MDFs for small R_{gal} , the mode does shift to lower abundances, but not to the same extent as in the observed sample, and with minimal change in skewness. Although the model predicts a portion of the effect, it cannot account for the entire $|z|$ -dependence of the MDF shape in the inner Galaxy.

3.3 $[\text{O}/\text{Fe}]$ distributions in Bins of $[\text{Fe}/\text{H}]$

In this section we compare our predicted $[\text{O}/\text{Fe}]$ distributions in various Galactic regions to those recently published in [Vincenzo et al. \(2021a\)](#). As in our § 3.2, they also make use of APOGEE DR16 ([Ahu-mada et al. 2020](#); [Majewski et al. 2017](#)), and impose

a similar set of cuts on effective temperature, surface gravity, and signal-to-noise (see their § 2). These distributions are estimates of the *intrinsic* [O/Fe] distributions that, when convolved with observational uncertainties and the APOGEE selection function, would resemble the observed MDFs like those in [Hayden et al. \(2015\)](#). We show the distributions predicted by our fiducial model in $\Delta[\text{O/Fe}] = 0.04$ bins across 15 Galactic regions in comparison to the [Vincenzo et al. \(2021a\)](#) distributions shown in dashed lines in Fig. 12. Galactic regions are defined by a range in R_{gal} , shown in columns and denoted at the top of the figure, and a range in $|z|$, shown in rows and denoted in text in the left-hand column. We show this comparison for two bins in [Fe/H], colour-coded according to the legend in the top-right panel.

Finding similar results for all of our SFHs, we note that our model adequately reproduces the broad nature of the [O/Fe] distributions at fixed [Fe/H] seen in the APOGEE data. Some distributions in a specific Galactic region and [Fe/H] bin show a bimodality in decent agreement with the observations (e.g. the $-0.4 \leq [\text{Fe/H}] \leq -0.2$ bin at $R_{\text{gal}} = 7 - 9$ kpc and $|z| = 1 - 2$ kpc), but this is not true of all Galactic regions in both metallicity bins. Instead, the principle failure of our model is that it overpredicts the number of intermediate [O/Fe] stars.

In the inner Galaxy, our model overestimates the mode [O/Fe] to some extent for both [Fe/H] bins, but the difference is larger for the higher of the two. This discrepancy also increases with increasing $|z|$. At fixed R_{gal} , the [Vincenzo et al. \(2021a\)](#) distributions show two peaks which do not change with $|z|$; only their relative heights vary. This is an assumption built into the model, but the agreement with the APOGEE data is good. However, this is a region of the Galaxy where there aren't many APOGEE stars. At $|z| = 1 - 2$ kpc for $R_{\text{gal}} = 3 - 5$ and $5 - 7$ kpc, the [Vincenzo et al. \(2021a\)](#) model is fit to 31 and 17 stars, respectively. In comparison, there are 109 in the solar annulus, and all other bins have >75 stars involved in the fit. It's possible the observed distributions shift slightly to higher $[\alpha/\text{Fe}]$, but at most at the $\lesssim 0.05$ level (see their Fig. 11).

If this discrepancy persists in subsequent APOGEE data releases which will better characterize the distributions in these regions, it's possible the origin is tied to the Sagittarius dwarf. The h277 simulation, which drives stellar migration in our models (see discussion in §2), did not have such an accretion event. With its most recent major merger occurring at a redshift of $z \approx 3$, this galaxy has previously been selected for investigation expressly because of its quiescent merger history (e.g. [Zolotov et al. 2012](#)). N-body models for the tidal disruption of the Sagittarius dwarf, on the other hand, suggest pericentric passages around 6.5, 4.5, 2.75, 1, and 0.1 Gyr ago ([Law & Majewski 2010](#)). In addition to potentially triggering episodes of star formation (e.g. [Ruiz-Lara et al. 2020](#)), more frequent pericentric passages of a massive satellite could kinematically heat low- $[\alpha/\text{Fe}]$ disc stars to higher $|z|_{\text{max}}$ orbits. Such effects are not a component of the dynamical history of h277; this is one instance where running our models with a different hydrodynamical simulation's star particles may be an enlightening comparison.

The notion that an $[\alpha/\text{Fe}]$ dichotomy can arise out of radial migration alone traces back to [Schönrich & Binney \(2009\)](#), and was later explored by [Nidever et al. \(2014\)](#) and recently by [Sharma et al. \(2020\)](#). This however suggests that an inside-out star formation history combined with stellar migration is not conducive to predicting this observed result, even when a recent starburst is added. The primary failure being an overpredicted frequency of intermediate $[\alpha/\text{Fe}]$ stars, this could point to a number of things. If the bimodality is to arise out of inside-out Galaxy evolution and stellar migration alone, then the transition between high- and low- α sequences needs

to occur faster than it does in these models. The analytic arguments of [Weinberg et al. \(2017\)](#) suggest that the approach to equilibrium occurs on the order of the SFE timescale τ_{\star} (see § 2.5). Since we've adopted a star formation law which is motivated by observational results, the failure of these models to reproduce the observed dichotomy suggests that the typical SFE timescales as observed are not short enough to explain such a fast transition. This would imply that either the Milky Way occupied a special place in the scatter of the observed $\dot{\Sigma}_{\star} - \Sigma_{\text{g}}$ relation at a time early in its evolutionary history, or the bimodality arose out of alternative pathways. Under our current assumptions, the simplest way to decrease the frequency of intermediate $[\alpha/\text{Fe}]$ stars is to simply shut off (or turn down) star formation when the ISM is at such a composition. This is an indication that two-infall evolutionary histories (e.g. [Chiappini et al. 1997, 2001](#); [Romano et al. 2010](#); [Grisoni et al. 2017](#); [Noguchi 2018](#); [Palla et al. 2020](#); [Spitoni et al. 2016, 2018, 2019, 2020, 2021](#)) would improve the agreement between our model predictions and the observed distributions.

3.4 The Age- $[\alpha/\text{Fe}]$ Relation

In this section, we assess the predicted age-[O/Fe] relations of our models, using the results of [Feuillet et al. \(2019\)](#) as the observational benchmark; their stellar age measurements are based on isochrone matching. While we made use of APOGEE DR16 data in comparing our model predictions to the observed MDFs ([Ahumada et al. 2020](#); [Majewski et al. 2017](#), see § 3.2), they made use of APOGEE DR14 stars for which parallax measurements are available from Gaia ([Abolfathi et al. 2018](#); [Gaia Collaboration et al. 2018](#)). With their spatial and quality cuts, the final sample consisted of 77,562 stars. In bins of [O/Fe], they assume a gaussian log age distribution, fitting the mean and standard deviation to the stars in that bin. Because they assume a gaussian, they would report an equal mean and median log age. This means that a one-to-one comparison of our model predictions to their results is not free of nuance, because they predict log age distributions which are highly non-gaussian at fixed [O/Fe].

The stellar populations from our simulations have different masses; this necessitates weighting the age-distributions by present-day mass, because that scales with the number of stars that a model stellar population represents. We therefore adopt the 50th percentile of the mass-weighted age distribution in a bin of [O/Fe] as the characteristic age to compare to the [Feuillet et al. \(2019\)](#) measurements. We refer to this quantity as the mass-weighted median age.

In the left-hand set of panels of Fig. 13, we compare the age-[O/Fe] relation in the solar annulus ($R_{\text{gal}} = 7 - 9$ kpc and $|z| \leq 0.5$ kpc) predicted by our four migration models to the [Feuillet et al. \(2019\)](#) measurements, shown in red triangles. We mark the mass-weighted median age in bins of [O/Fe] in each model with black squares, and plot for reference in the background each individual stellar population in the solar annulus, colour-coded according to its Galactocentric radius of birth.

We note that the inside-out SFH, assumed by all four of the models illustrated here, provides a reasonable description of the age-[O/Fe] relation as observed in APOGEE. We also note that each model for the time-dependence of stellar migration predicts differing amounts of scatter in the age-[O/Fe] relation. Diffusion has the most, followed by linear, then sudden, and lastly post-processing. We interpret this as a consequence of the variability in the SN Ia rate as a function of radius and time caused by time-dependent migration (see Fig. 8 and associated discussion near the beginning of §3). When the SN Ia rate is higher or lower than expected given the

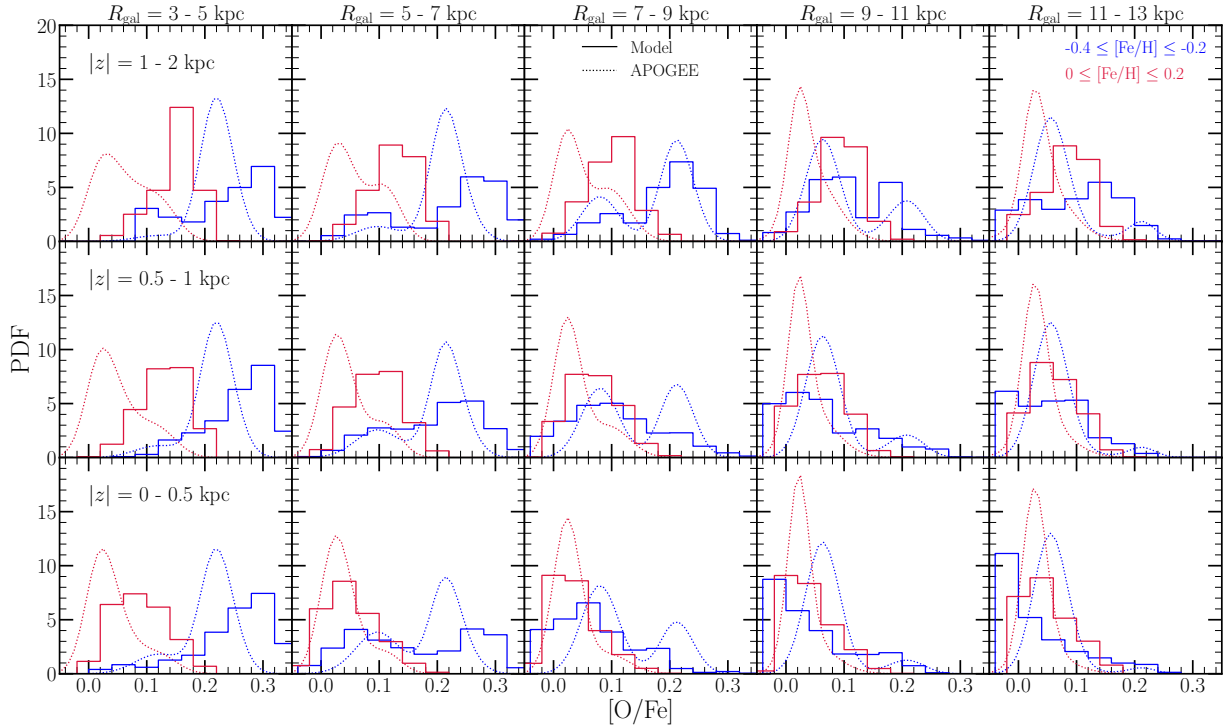


Figure 12. Predicted distributions in $[O/Fe]$ in 15 Galactic regions and in two bins in $[Fe/H]$. Columns correspond to bins in R_{gal} , denoted at the top of each column. Rows correspond to bins in $|z|$, denoted in text in the left-hand column. Distributions are color-coded according to the $[Fe/H]$ the sample is drawn from, denoted by the legend in the upper right panel. Solid lines represent that predicted by our inside-out SFH in $\Delta[O/Fe] = 0.04$ bins, while dashed lines correspond to the fits to the APOGEE DR16 data presented in Vincenzo et al. (2021a), which quantify the intrinsic distributions accounting for observational uncertainties and the APOGEE selection function.

SFH of an annulus, then the Fe abundance in that zone will increase or decrease accordingly. This can occur if there is a significant net gain or loss of SN Ia progenitors in a given time interval due to time-dependent migration. The gas-phase $[O/Fe]$ then decreases or increases in turn, and the stars which form out of that gas inherit these compositions. When migration is taken into account and stellar populations are mixed as a consequence, the observational signature is intrinsic scatter in the age- $[\alpha/Fe]$ relation.

All of the models in the left-hand set of panels predict a correlation between mass-weighted median age and $[O/Fe]$ in good agreement the Feuillet et al. (2019) measurements assuming the inside-out SFH. This suggests that the population averaged trend is unaffected by stellar migration. However, only the diffusion and linear migration models predict a population of young ($\lesssim 4$ Gyr), $[\alpha/Fe] \approx +0.1 - 0.2$ stars in the solar neighbourhood. These stars are a part of the noticeable upward scatter in the relationship, and we therefore interpret their origin to be the same as the scatter itself - they formed in a region of the Galactic ISM at a time when it was particularly alpha-enhanced due to a rather lasting deficit in SN Ia events. These stars then migrated to the solar annulus, where they showed up in the APOGEE data when stellar ages were measured using carbon-to-nitrogen ratios (Martig et al. 2016), isochrone matching (Feuillet et al. 2018, 2019), and with the asteroseismic ages of the origin APOKASC catalog (Chiappini et al. 2015; Silva Aguirre et al. 2018; Pinsonneault et al. 2014).

Silva Aguirre et al. (2018) demonstrate that the observed young α -rich stars in the solar annulus have kinematics similar to the rest of the high- α population, and suggested this may be the result of stellar mergers or mass transfer events. This would produce a population of

truly old stars masquerading as young stars. In a sample of 51 young, α -rich red giants, Hekker & Johnson (2019) demonstrate that a portion of these stars have carbon-to-nitrogen ratios consistent with mass transfer events, but that others do not, indicating they’re either truly young stars or the result of mergers on the main sequence. As far as we know, the mechanism discussed here is the first theoretical explanation of the origin of these stars. We note additionally that under this explanation, the young α -rich stars are not so much α -rich as they are Fe-poor, and form overwhelmingly at large R_{gal} where the SN Ia rate is most variable (see discussion in § 3.1).

In the right-hand set of panels in Fig. 13, we compare the model predictions of our four different SFHs, assuming our diffusion migration model, with the same plotting scheme and colour-coding as in the left-hand panels. We note that the constant and inside-out SFHs describe the data the best. Although our e-folding timescales for star formation are sufficiently long at large R_{gal} such that there is little difference between the constant and inside-out SFHs there anyway (see discussion in § 2.4), our constant SFH is idealized and of purely theoretical interest, making the inside-out model the more likely of the two. Below $[O/Fe] \approx +0.1$, the Feuillet et al. (2019) data seem to follow a slightly steeper age- $[\alpha/Fe]$ relation than our inside-out model predicts. This could point to any number of things being an inaccuracy in our models: the detailed form of the SFH or the SN Ia DTD, our supernova yields, or observational $[O/Fe]$ errors, all of which are plausible.

We note that our starburst models, both late-burst and outer-burst, disagree with the Feuillet et al. (2019) measurements. The late starburst produces a population of young, α -rich stars due to the perturbed ratio of core collapse to type Ia supernova rates (John-

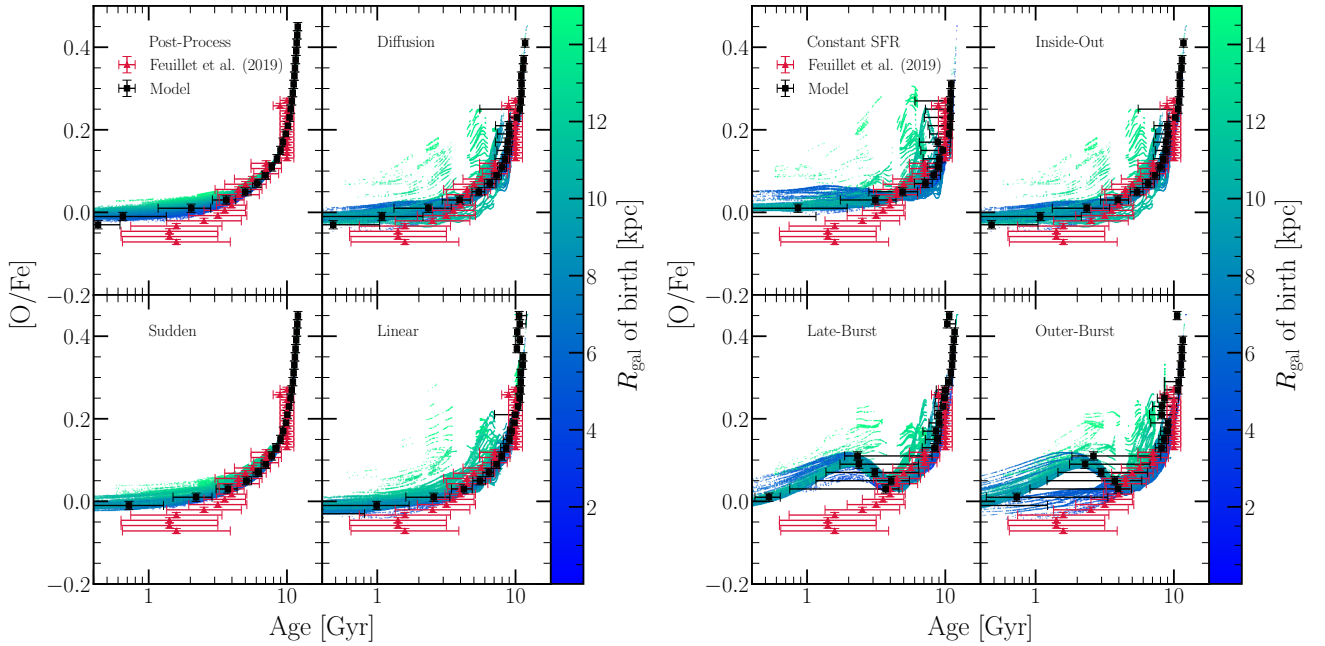


Figure 13. **Left:** A comparison of the predicted age-[O/Fe] relation for the solar annulus ($R_{\text{gal}} = 7 - 9$ kpc and $|z| = 0 - 0.5$ kpc) between the post-processing (upper left), diffusion (upper right), sudden (lower left), and linear (lower right) migration models, assuming our inside-out SFH. **Right:** The same as the left-hand panels, instead comparing the impact of our constant (upper left), inside-out (upper right), late-burst (lower left), and outer-burst (lower right) SFHs, assuming diffusion migration. In all panels, red triangles and error bars denote the observed mean age and dispersion thereof in bins of [O/Fe] as reported by Feuillet et al. (2019); here we include only the bins containing at least 15 stars. Black squares denote the mass-weighted median age in 0.02-dex bins in [O/Fe] predicted by our models, with error bars denoting the 16th and 84th percentiles of the mass-weighted age distribution in those bins. Points in the background denote each individual stellar population from the model with a final position in the solar annulus, colour-coded according to their Galactocentric radius of birth.

son & Weinberg 2020). With the starburst occurring in a substantial fraction of the ISM in both models, the result is an increase in the bulk $[\alpha/\text{Fe}]$ for young stars which simply is not seen in the observed sample. The effect is strong enough that at $[\text{O}/\text{Fe}] \approx +0.1$, both models considerably overpredict the width of the distribution, simultaneously predicting a mass-weighted median age many times the standard deviation younger than observed. This discrepancy is of interest, because these models were motivated by the observational results of Mor et al. (2019) and Isern (2019) which suggest such a recent starburst. Although our functional forms differ from what they reported in detail, they’re reasonable descriptions of the measurements within the error bars. This suggests that the results of Mor et al. (2019) and Isern (2019) are at odds with chemical evolution models of the Milky Way. If the Galaxy truly experienced a recent starburst, then something not included in our models had to prevent this global increase in $[\alpha/\text{Fe}]$.

In Fig. 14, we extend the comparison of our base-line, inside-out model and the observations of Feuillet et al. (2019) to other Galactic regions. We visualize the data there in the same manner as for previous figures in this section. While the inside-out model shows the best agreement with the observed result in the solar annulus, there are some mild discrepancies for stars farther from the sun. Feuillet et al. (2019) report ages for α -rich stars that are younger at large R_{gal} and high $|z|$, though in most cases only by $\sim 20\%$. Our model does not capture this effect. To illustrate this, we connect the black squares in the panel corresponding to the solar annulus with a black line, and then reproduce this line in all panels for reference. If the observational result is correct, this is an interesting effect that our model doesn’t reproduce in any of the variants we’ve explored. Furthermore, we note that the model overpredicts ages at large $|z|$.

As with the overpredicted [O/Fe] ratios at small R_{gal} , we speculate that this may be tied to the Sagittarius dwarf (see discussion in § 3.3). By using a hydrodynamical simulation of a galaxy which exhibited more pericentric passages of a massive satellite, more young stars may be kinematically heated to high $|z|_{\text{max}}$ orbits. This is another instance where running our models with a different hydrodynamical simulation’s star particles may be an enlightening comparison.

We note that the intrinsic scatter in the age-[O/Fe] relation is predicted to grow with increasing R_{gal} ; this can be seen in the error bars on the black squares as well as the coloured points. We identify two sources of this dependence; the bulk of the scatter, at least at $[\text{O}/\text{Fe}] \gtrsim +0.05$, arises from the variability in the SN Ia rates as described in § 3.1. Having demonstrated that the SN Ia rate is most variable at large R_{gal} , the in-situ populations in the outskirts of the Galactic disc formed from an ISM whose gas-phase [O/Fe] ratio varied with a higher amplitude. Since the observational signature of this variability is scatter in the observed age-[O/Fe] relation, our model predicts the most intrinsic scatter in Galactic regions where that variability has the highest amplitude. Second, the analytic models of Weinberg et al. (2017) suggest that as the e-folding timescale for star formation τ_{sff} increases, the model-predicted [O/Fe] of the youngest stars increases with a weak dependence. With a range of e-folding timescales in our model, this implies a distribution of [O/Fe] at age = 0 with nonzero width without considering the migration of nucleosynthetic yields. This can be seen in the post-processing model predicted age-[O/Fe] relation in Fig. 13. In this pathway, scatter is induced by mixing populations that follow age-[O/Fe] relations of slightly different normalizations which are nearly flat intrinsically, producing a noticeably wide age distribution near solar [O/Fe].

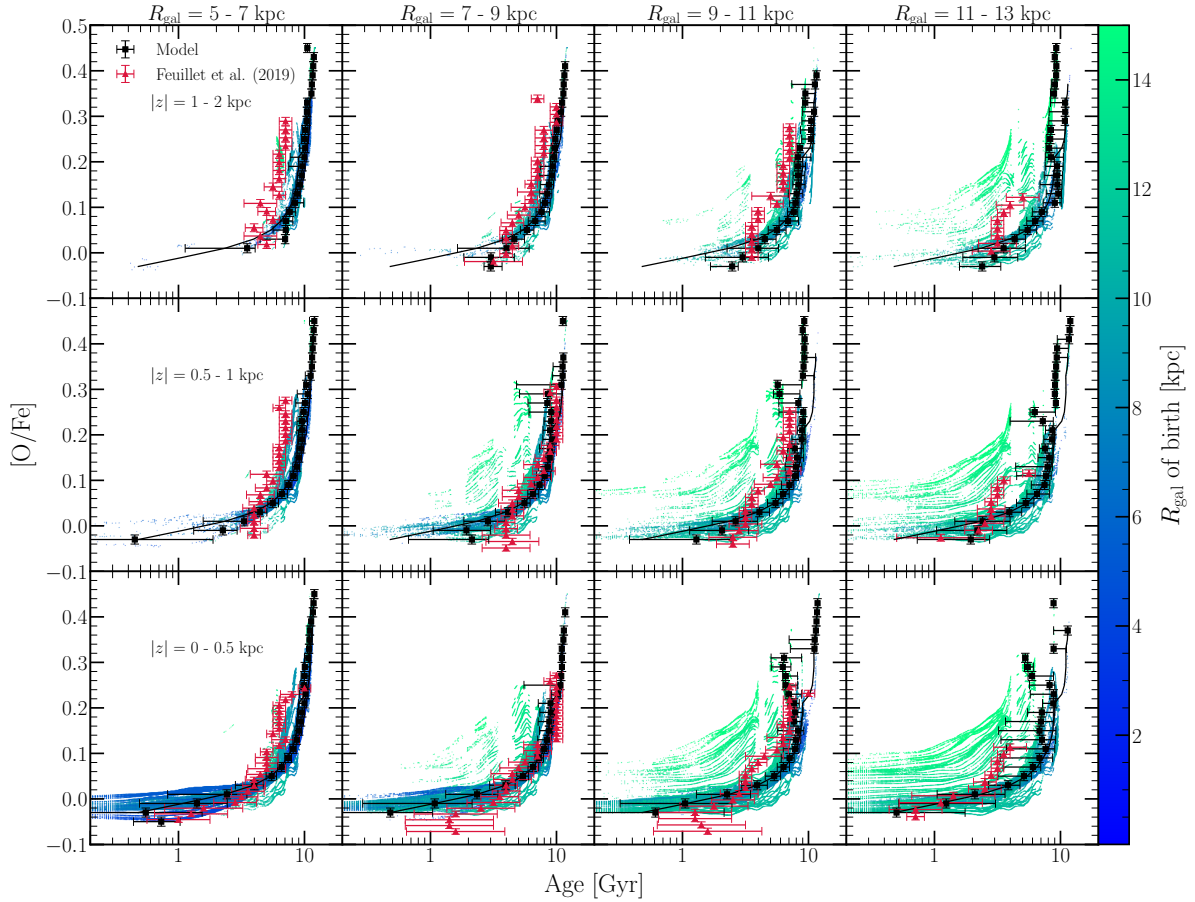


Figure 14. The age-[O/Fe] relation in 12 Galactic regions predicted by our inside-out SFH. Bins in Galactocentric radius are shown in columns, and labeled at the top. Bins in the height $|z|$ above/below the disc midplane are shown in rows, noted in the left-hand column. Red triangles, black squares, error bars, and background points are as in Fig. 13 for the corresponding Galactic region. The solid black line connects the black squares in the bottom, left-middle panel, and is replicated elsewhere for reference.

Although the iron-peak is the only class of elements with a delayed nucleosynthetic source that we consider in the present paper, we expect similar results for other delayed sources with regard to the variability in enrichment rates and scatter in age-[X/Y] relations. The details of SN Ia nucleosynthesis did not matter in our interpretations in this section; it is based purely on the characteristic delay-times of the source and how they compare to the timescales of stellar migration. Our models should then find similar predictions with, for example, s-process (slow neutron capture) elements like carbon, nitrogen, strontium, yttrium, and zirconium produced in asymptotic giant branch stars. In fact, using hydrodynamical simulations from the Auriga project (Grand et al. 2017), van de Voort et al. (2020) find that the intrinsic scatter in r-process (rapid neutron capture) abundances increases for models with longer characteristic delay times. Although the first observations of a binary neutron star merger (GW170817) exhibited an optical counterpart which was consistent with being powered by the radioactive decay of r-process elements (Abbott et al. 2017; Coulter et al. 2017; Drout et al. 2017; Pian et al. 2017), it remains unclear the extent to which neutron star mergers contribute to r-process nucleosynthesis in the universe (Côté et al. 2019; Mishenina et al. 2019; Siegel 2019; van de Voort et al. 2020; Vincenzo et al. 2021b). Although it's likely unfeasible at present due to the requirement for high precision abundance measurements of intrinsically rare elements in

many stars, with future observational capabilities, the application of our results as well as van de Voort et al. (2020) suggests that the intrinsic scatter in r-process abundances may provide constraints on the characteristic delay times of such nucleosynthetic events.

3.5 The Age-Metallicity Relation

Although the age-metallicity relation (AMR) is usually formulated in terms of $[\text{Fe}/\text{H}]$, it is also interesting to quantify the age-[O/H] relation, because it is not affected by SN Ia enrichment. The extent to which they differ indicates the extent to which the delayed timescale and impact of migration on SN Ia enrichment is important in shaping the age-[Fe/H] relation. In Fig. 15, we present the age-[O/H] relation predicted by our constant SFH model for the $|z| \leq 0.5$ kpc population at $R_{\text{gal}} = 7 - 9$ and $11 - 13$ kpc. The black squares with error bars denote the mass-weighted median age as in § 3.4, and we again plot the individual stellar populations in the background for reference, colour-coded according to their Galactocentric radius of birth. We omit the Feuillet et al. (2019) measurements from this figure, because the constant SFH model is of purely theoretical interest, removing the effects of a time-varying SFH while including the effects of stellar migration.

The intrinsic scatter in the observed AMR has previously been interpreted as evidence for radial mixing (Edvardsson et al. 1993;

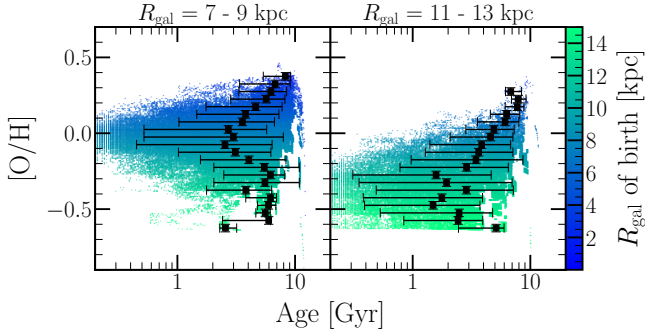


Figure 15. The age-[O/H] relation predicted by our constant SFH model for $R_{\text{gal}} = 7 - 9$ kpc (left) and $11 - 13$ kpc (right). Each panel plots only the $|z| \leq 0.5$ kpc population. The colored points in the background and the black squares with error bars are as in Fig. 13, but with our binned, model prediction quantified in bins of $\Delta[\text{O}/\text{H}] = 0.05$.

Sellwood & Binney 2002). In the solar neighbourhood, Feuillet et al. (2018) demonstrate that the most metal-rich stars tend to be significantly older than solar metallicity stars. Using the Weinberg et al. (2017) analytic models of one-zone chemical evolution, they argue that this is the result of old stars born at small R_{gal} where the equilibrium abundance is high. Only the old stars are able to migrate to the solar neighbourhood due to the time required for such a change in their orbital radius.

The results of our constant SFH model illustrated in Fig. 15 extend our understanding of this effect. In both regions plotted, the youngest stars form with a composition inherited from the local ISM, which in this model, is reflective of the late-time equilibrium abundance. At a given age, only stars born in a well-defined region of the Galaxy will have had adequate time to migrate to a given present-day radius. Since a range of R_{gal} maps directly to a range of metallicity once the ISM is arbitrarily close to the equilibrium abundance in our model, this necessitates a maximum width of the [O/H] distribution at fixed age. With increasing age, the [O/H] distribution then gets wider because any given present-day radius samples stars formed at a wider range of R_{gal} . In Fig. 15, we indeed see this effect, with the colour-coding of the background points making it clear that stellar migration is the culprit. In the outer Galaxy, migration has a particularly interesting effect in that it only adds old stars above the equilibrium metallicity; in the $R_{\text{gal}} = 11 - 13$ kpc region, our model as a consequence predicts an AMR where the population-averaged trend where [O/H] is nearly monotonically increasing with age. This is entirely backwards from what is expected from one-zone models of GCE (e.g. Andrews et al. 2017; Weinberg et al. 2017; Johnson & Weinberg 2020).

We continue our assessment of the model-predicted AMR by illustrating in Fig. 16 the age-[O/H] (top) and age-[Fe/H] (bottom) relations predicted for the solar annulus (i.e. $R_{\text{gal}} = 7 - 9$ kpc and $|z| \leq 0.5$ kpc). The red triangles, black squares, coloured points, and error bars are as in previous figures in §3.4. For reference, we add the solid dark red line, which denotes the AMR measured by Feuillet et al. (2018). Although our model shows decent agreement with the Feuillet et al. (2019) measurements in the solar annulus, Feuillet et al. (2018) report ages for solar metallicity stars which are considerably younger ($\sim 1 - 2$ Gyr as opposed to $\sim 3 - 4$ Gyr). The Feuillet et al. (2018) data would suggest our inside-out model requires an enhancement in the recent SFR to increase the frequency of young, solar metallicity stars. Although our late-burst and outer-burst mod-

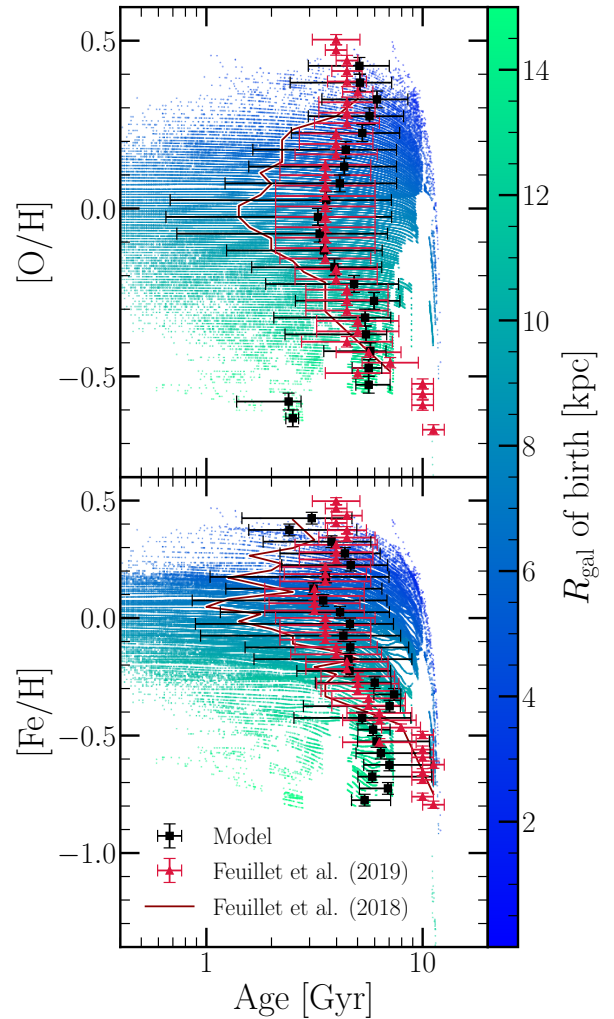


Figure 16. The age-[O/H] (top) and age-[Fe/H] (bottom) relations for the solar annulus (i.e. $R_{\text{gal}} = 7 - 9$ kpc, $|z| \leq 0.5$ kpc) as predicted by our inside-out SFH. Red triangles, black squares, error bars, and background points are as in Fig. 13, but with our model predicted quantified in bins of $\Delta[\text{O}/\text{H}] = \Delta[\text{Fe}/\text{H}] = 0.05$. For comparison, we plot the Feuillet et al. (2018) measurements in a dark red line, omitting the associated uncertainties for visual clarity.

els include such effects, motivated by recent observations suggesting this exact evolutionary history (Mor et al. 2019; Isern 2019), the differences between the Feuillet et al. (2018) and Feuillet et al. (2019) measurements are interesting in and of themselves.

Motivated by this, we compare the predictions of the inside-out and late-burst SFH models to the Feuillet et al. (2019) age-[Fe/H] relation in Fig. 17. We retain the same plotting scheme used throughout this section and § 3.4, illustrating the inside-out model in the top row and the late-burst model in the bottom row. Each column corresponds to a specific range in R_{gal} , denoted at the top of the figure. Beyond the solar annulus, we note that our inside-out model has a number of short-comings in comparison to the Feuillet et al. (2019) measurements. At $R_{\text{gal}} = 5 - 7$ kpc, it overpredicts the characteristic ages of $[\text{Fe}/\text{H}] \approx -0.3 - 0$ stars. At $R_{\text{gal}} = 9 - 11$ and $11 - 13$ kpc, it mildly overpredicts ages at most abundances, and fails to reproduce the trend seen in the observed sample. The same can be said about the $R_{\text{gal}} = 5 - 7$ kpc region, and although the overall

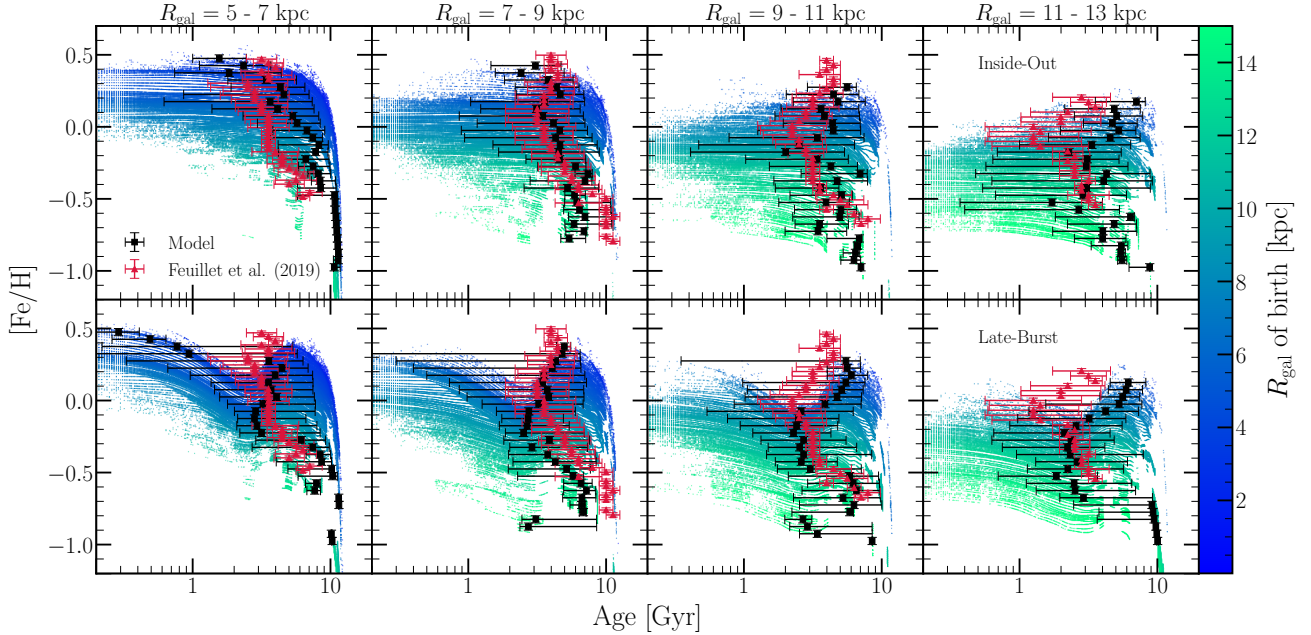


Figure 17. The age-[Fe/H] relation predicted by our inside-out (top) and late-burst (bottom) SFHs for $R_{\text{gal}} = 5 - 7$ kpc (left), $7 - 9$ kpc (left middle), $9 - 11$ kpc (right middle), and $11 - 13$ kpc (right). Each panel shows only the $|z| \leq 0.5$ kpc population. Red triangles, black squares, error bars, and coloured points are as in Fig. 13 for the corresponding Galactic region, but with our model prediction quantified in bins of $\Delta[\text{Fe}/\text{H}] = 0.05$.

agreement is generally good there, one could reasonably argue this for the solar annulus as well.

The late-burst model improves upon these shortcomings of the inside-out model considerably. At $R_{\text{gal}} = 5 - 7$ kpc, the overpredicted ages at solar and mildly sub-solar $[\text{Fe}/\text{H}]$ is no longer present; this is also true at $R_{\text{gal}} = 9 - 11$ and $11 - 13$ kpc. Furthermore, the trend is much better reproduced at all radii in the late-burst than the inside-out model. The only difference between the late-burst and inside-out model being the recent enhancement in the SFR, this is what drives the differences in model predictions. To fuel the starburst as we have parameterized it, VICE calculates that there must be substantial gas accretion (see the infall rate $\dot{\Sigma}_{\text{in}}$ as a function of radius and time in Fig. 4). In our models, we assume accretion to always be of zero metallicity gas. As a result, the model predicts dilution of the ISM Fe abundance during the starburst; this can be seen by the trend of the coloured points in Fig. 17 to lower $[\text{Fe}/\text{H}]$ at ages of $\sim 2 - 3$ Gyr. At this time, the star formation rate is elevated by construction. The net effect is to increase the frequency of $\sim 2 - 3$ Gyr old stars with near- and sub-solar abundances globally, which lowers the characteristic ages of stars at these metallicities relative to the inside-out model. Using the Feuillet et al. (2019) measurements as the observational benchmark, we favor the late-burst model here.

Although there appears to be a vertical offset between the observed result and the model prediction at $R_{\text{gal}} = 9 - 11$ and $11 - 13$ kpc, this is still an improvement upon the inside-out model. It's possible that this points to a need for higher yields of Fe than we've adopted here, though it's unclear if this would negatively affect the agreement at $R_{\text{gal}} = 5 - 7$ and $7 - 9$ kpc. It's possible that our parameterization of the mass-loading factor η scales too strongly with R_{gal} in the outer Galaxy (see discussion in § 2.3). Alternatively, outflows in nature may be more efficient at removing some elements from the ISM than others; this could impact the

overall normalization of the AMR at different radii. Our models in the present paper assume that outflows always proceed exactly at the metallicity of the ISM, but some authors argue that outflows can have a different metallicity - usually a higher one - due to containing in some part the metal-rich supernova ejecta that was added directly to the outflow by the explosions (observationally: Chisholm, Tremonti & Leitherer 2018; in simulations: Christensen et al. 2018).

We also note that the late-burst model predicts particularly young characteristic ages for the most metal-rich bins at $R_{\text{gal}} = 5 - 7$ kpc. This is purely a consequence of our choice to use the mass-weighted median as the population-averaged age measurement at fixed abundance. In this case, our model is simply reporting the 50th percentile of an age-distribution which is noticeably bimodal; as a result, whether or not the characteristic ages we report there are < 1 Gyr or in better agreement with the Feuillet et al. (2019) measurements strongly depends on how we've parameterized the recent starburst as a function of both time and radius. Here we've made the simplest assumption of letting have the same time-dependence at all radii, which was not necessarily the case.

Although we demonstrate here that the late-burst model describes the age-[Fe/H] relation reported by Feuillet et al. (2019) better than the inside-out model, we found the exact opposite with regard to the age- $[\alpha/\text{Fe}]$ relation with the same observational sample in § 3.4. It's unlikely this discrepancy can be mitigated using any model which exhibits a recent starburst as parameterized here; as we demonstrated in § 3.4, such models predict a global increase in $[\alpha/\text{Fe}]$ due to the perturbed ratio of CCSN and SN Ia rates (Johnson & Weinberg 2020), a feature which simply isn't seen in the Feuillet et al. (2019) measurements. It's possible that the Milky Way experienced dilution with no ensuing starburst - this would be the case if the majority of the accreted gas was warm, neutral and ionized gas which simply hasn't yet been made available for star forma-

tion. Such a scenario would exhibit some of the predictions of the late-burst model, but without the increase in $[\text{O}/\text{Fe}]$ at late times, potentially allowing it to simultaneously explain the age- $[\alpha/\text{Fe}]$ relation and AMR as they are observed. However, these models would be at odds with the findings of [Mor et al. \(2019\)](#) and [Isern \(2019\)](#).

We remark that we find similar results for the age- $[\text{O}/\text{H}]$ relation; furthermore, as in § 3.4 for the age- $[\alpha/\text{Fe}]$ relation, we also find for the age- $[\text{Fe}/\text{H}]$ and age- $[\text{O}/\text{H}]$ relations that our models tend to overpredict ages with increasing $|z|$. Lastly, we caution future studies against basing the likelihood of a chemical evolution model on data for the solar annulus alone. In Fig. 16, we noted that there was decent agreement between the inside-out SFH model and the [Feuillet et al. \(2019\)](#) measurements of the age- $[\text{O}/\text{H}]$ and age- $[\text{Fe}/\text{H}]$ relations in the solar annulus, but upon extending the comparison to other Galactic regions in Fig. 17, a number of shortcomings revealed themselves. Although to some extent this is made possible only recently with observational capabilities now allowing statistical measurements of these correlations for stars at greater distances from the sun, had we stopped there, we would have missed this interesting and peculiar result.

4 DISCUSSION & CONCLUSIONS

In this paper, we have modeled the Milky Way as a series of concentric annuli with a $\Delta R_{\text{gal}} = 100$ pc width, describing each annulus as a conventional one-zone chemical evolution model and allowing the exchange of stellar populations between zones to include the impact of stellar migration in the model Galaxy. Though there have been a handful of studies which employ a similar methodology ([Schönrich & Binney 2009](#); [Nidever et al. 2015](#); [Sharma et al. 2020](#)), ours and the [Minchev et al. \(2013, 2014, 2017\)](#) model are the only ones which make use of a hydrodynamical simulation to describe radial mixing, for which we make use of the h277 zoom-in simulation ([Christensen et al. 2012](#); [Zolotov et al. 2012](#); [Loebman et al. 2012, 2014](#); [Brooks & Zolotov 2014](#)). This yields a model for migration which does not have any free parameters (see discussion in §2.1).

Our model predicts masses and abundances for simple stellar populations, a given number of which form at each timestep. Each stellar population is then assigned a star particle from h277 which was born at a similar radius and time to act as an *analog*. The stellar population in our model then assumes the change in radius ΔR_{gal} of the analog at face value, and is assumed to reside at the same present day height above/below the disc midplane $|z|$. We then construct four models describing the time-dependence with which stellar populations move to their present-day radii, taking one in which radius changes with a $\sqrt{\text{age}}$ -dependence in the fiducial model based on [Frankel et al. \(2018, 2020\)](#), see Fig. 2 and discussion in §2.2).

We assume SN yields and a SN Ia delay-time distribution based on a combination of theoretical and empirical constraints. The main free parameters are the star formation law parameterizing the SFE timescale τ_* (see discussion in § 2.5), the mass-loading factor $\eta(R_{\text{gal}})$ describing the strength of outflows (assumed to be time-independent; see discussion in § 2.3), and the SFH. The first we choose from the observed $\dot{\Sigma}_* - \Sigma_g$ relation in local spirals ([Bigiel et al. 2010](#); [Leroy et al. 2013](#); [Krumholz et al. 2018](#)). The second is chosen to reproduce the metallicity gradient as observed ([Daflon et al. 2009](#); [Frinchaboy et al. 2013](#); [Hayden et al. 2014](#); [Weinberg et al. 2019](#)). Our fiducial model then has an inside-out SFH with e-folding timescales calibrated to the [Sánchez \(2020\)](#) data (see dis-

cussion in § 2.4). Motivated by the results of [Mor et al. \(2019\)](#) and [Isern \(2019\)](#) suggesting such an evolutionary history, we construct models which exhibit a recent burst in star formation on top of the base-line model, as well as a constant SFH model of purely theoretical interest.

We find that when stellar migration proceeds in a manner in which a star's orbital radius changes continuously with time, the SN Ia rate as a function of both radius and time exhibits significant variability. The characteristic delay time of a single SN Ia event is ~ 1 Gyr ([Maoz & Mannucci 2012](#); [Maoz & Graur 2017](#)), and stars are migrating a significant distance in the radial direction on similar timescales in our models. The result is a SN Ia rate which, at fixed radius, tends to follow that which is expected from the SFH when averaged with time, but whose instantaneous value may be considerably larger or smaller. Our model predicts the amplitude of this variability to grow with increasing radius due to sampling noise and the inverse dependence of the stellar surface density on R_{gal} . We demonstrate that this is a mechanism with which truly young, super-solar $[\alpha/\text{Fe}]$ stars can form. When the SN Ia rate increases or decreases, the Fe abundance in the ISM increases or decreases accordingly; this in turn affects the gas-phase $[\alpha/\text{Fe}]$ ratio, and the stars which form at these times inherit these compositions. Of the young stars, those with the highest $[\alpha/\text{Fe}]$ form at large R_{gal} ($\gtrsim 12$ kpc) due to the radial dependence of the amplitude; a subsample of these stars can then migrate to the solar annulus.

To our knowledge, this mechanism lends the first theoretical explanation of truly young α -rich stars in the solar neighbourhood, revealed recently by the observations of the APOGEE survey ([Martig et al. 2016](#); [Feuillet et al. 2018, 2019](#); [Silva Aguirre et al. 2018](#)). [Silva Aguirre et al. \(2018\)](#) find that these stars have kinematics consistent with the rest of the high- α population, and postulate based on this that these stars are the consequence of stellar mergers or mass transfer events, making truly old stars simply appear younger. In a sample of 51 young α -rich red giants, [Hekker & Johnson \(2019\)](#) demonstrate using carbon-to-nitrogen ratios that a portion of these stars are indeed old, but that these effects cannot account for the entire population. We argue based on our results that the truly young ones formed at large R_{gal} at a time when the ISM was intrinsically α -rich due simply to a deficit in SN Ia events caused by a net loss of white dwarf progenitors to stellar migration. We remark that our model would suggest that these stars have super-solar $[\alpha/\text{Fe}]$ not because they are α -rich, but rather that they are Fe-poor.

We find that our model adequately reproduces the variations in MDFs with Galactocentric radius in the disc ([Hayden et al. 2015](#)). Although there is a potential for improved agreement in the $R_{\text{gal}} = 3 - 5$ kpc bin, the model nonetheless performs well. With increasing $|z|$, the prediction breaks down somewhat. Where the observational data show a convergence of the MDFs at all radii to a skew-positive distribution with $\text{mode}([\text{O}/\text{H}]) \approx \text{mode}([\text{Fe}/\text{H}]) \approx -0.5$, our model predicts the mode abundance in the inner Galaxy to decrease slightly, though not to the same extent as in the observations, while the distributions at larger R_{gal} are less affected (see Figs. 10 and 11 and discussion in § 3.2). While the model accounts for a portion of these effects, it cannot explain the entire z -dependence of the MDF shape.

We demonstrate the dependence of the relative frequency of high- α and low- α sequence stars on Galactic position (see, e.g., Fig. 4 of [Hayden et al. 2015](#)) is at least in part a consequence of stellar migration. In our fiducial inside-out SFH model, low $[\text{Fe}/\text{H}]$, high $[\alpha/\text{Fe}]$ stars are the dominant population at small R_{gal} and high $|z|$; conversely, low $[\alpha/\text{Fe}]$ stars are most common at large R_{gal} and low $|z|$. We clarify that this is not an explanation for the *origin* of the two sequences - only the spatial dependence thereof. In fact, our

model is unable to account for the presence of the infamous $[\alpha/\text{Fe}]$ dichotomy in any of the variants we’ve explored. While it is able to reproduce the broad nature of the $[\text{O}/\text{Fe}]$ distributions at fixed $[\text{Fe}/\text{H}]$ and may show a convincing two-peaked profile in a specific Galactic region, it fails to do so for the entire Galaxy at all metallicities; the principle failure is an overpredicted frequency of intermediate $[\alpha/\text{Fe}]$ stars. This is in contrast to the findings of [Sharma et al. \(2020\)](#), who claim to reproduce the bimodality in a model assuming an inside-out SFH with stellar migration. However, they do not demonstrate that the enrichment history of their model follows self-consistently from their assumed SFH. We therefore argue that an inside-out SFH is not conducive to forming the abundance distributions observed in the Milky Way. Though we don’t investigate such evolutionary pathways in the present paper, our models fail in such a manner that suggests the agreement can best be improved by the three-phase SFH of the two-infall model ([Chiappini et al. 1997, 2001](#); [Romano et al. 2010](#); [Grisoni et al. 2017](#); [Noguchi 2018](#); [Palla et al. 2020](#); [Spitoni et al. 2016, 2018, 2019, 2020, 2021](#)). We reserve an investigation into more sophisticated forms of the Galactic SFH for future work.

We find that the age- $[\text{O}/\text{Fe}]$ relation as reported by [Feuillet et al. \(2019\)](#) is well-characterized by our inside-out SFH. In the case of our recent starburst models motivated by [Mor et al. \(2019\)](#) and [Isern \(2019\)](#), the elevation of the SFR necessitates an increase in $[\alpha/\text{Fe}]$ for young stars owing to the increased rate of CCSNe before the onset of SN Ia associated with the starburst ([Johnson & Weinberg 2020](#)), introducing a trend which simply isn’t seen in the observations. This suggests that recent studies finding an elevation in the Galactic SFR ~ 2 Gyr ago are at odds with chemical evolution models, which based on the monotonic nature of the observed AMR would put constraints on the amount of variability out to lookback times of ~ 8 Gyr. Lastly, we find that our model predicts the intrinsic scatter in the age- $[\alpha/\text{Fe}]$ relation to increase with R_{gal} ; this traces back to the variability in the SN Ia rates having a higher amplitude in the outer Galaxy, which produces an in-situ population with a larger dynamic range in $[\text{O}/\text{Fe}]$.

We find that the AMR (both age- $[\text{O}/\text{H}]$ and age- $[\text{Fe}/\text{H}]$) in the solar annulus as measured by [Feuillet et al. \(2019\)](#) is well-described by our inside-out SFH. However, when this comparison is extended to other Galactic regions, the inside-out model overpredicts ages in multiple regions and fails to reproduce the population-averaged trend throughout the disc. We demonstrate that our late-burst model can account for these discrepancies, suggesting that the observed AMR favors a model with a recent enhancement in the Galactic SFR. Somewhat confusingly, the impact of the late-burst model is such that it is convincingly rejected by the age- $[\text{O}/\text{Fe}]$ relation but convincingly favored by the age- $[\text{O}/\text{H}]$ and age- $[\text{Fe}/\text{H}]$ relations.

We thus conclude that no single model in the present paper can explain all of the observables of interest here. This suggests that conventional assumptions about the evolution of the Milky Way, such as an inside-out SFH with stellar migration, are not sufficiently accurate to understand the enrichment history of the Milky Way in detail. This is an indication that at present there is more astrophysical information in already collected observations than the most recent GCE models can explain. It’s likely our models are missing at least one key component with a significant impact on the predicted abundances.

Lastly, we remark on the low number of multi-zone chemical evolution models in the literature, some with and some without migration. In this paper, we present only a handful of models whose predictions can be calculated with a combined CPU-time comparable to a single working day. These models make straight-forward

predictions which can easily be compared to publicly-available observed data. Though they are extremely useful in many respects, these medium resolution, medium computational expense techniques can test assumptions about the evolutionary history of the Milky Way with more control over the parameters and much less computational expense than the higher overhead hydrodynamical simulations; our models here constitute an example of a combination of the two.

VICE is publicly available and open-source;¹ it can be installed in a Unix terminal via `pip install vice`. Python code which runs the simulations presented in this paper is included as supplementary material in the GitHub repository; our models can be ran directly from a terminal without modifying the source code, and are capable of predicting abundances for ~ 2 million stellar populations in ~ 2.5 CPU-hours running on a single core on personal computers.

5 ACKNOWLEDGEMENTS

We acknowledge valuable discussion with, in no particular order, Emily Griffith, Jennifer Johnson, Todd Thompson, Jiayi Sun, Amy Sardone, Adam Leroy, Grace Olivier, the Ohio State Astronomy Gas, Galaxies, and Feedback group, and various participants of the SDSS Gotham 2020 virtual collaboration meeting and the virtual 236th meeting of the American Astronomical Society. This work was supported in part by National Science Foundation grant AST-1909841. D.H.W. is grateful for the hospitality of the Institute for Advanced Study and the support of the W.M. Keck Foundation.

In this paper we have made use of data from SDSS-IV APOGEE-2 DR16. Funding for the Sloan Digital Sky Survey IV has been provided by the Alfred P. Sloan Foundation, the U.S. Department of Energy Office of Science, and the Participating Institutions.

SDSS-IV acknowledges support and resources from the Center for High Performance Computing at the University of Utah. The SDSS website is www.sdss.org.

SDSS-IV is managed by the Astrophysical Research Consortium for the Participating Institutions of the SDSS Collaboration including the Brazilian Participation Group, the Carnegie Institution for Science, Carnegie Mellon University, Center for Astrophysics | Harvard & Smithsonian, the Chilean Participation Group, the French Participation Group, Instituto de Astrofísica de Canarias, The Johns Hopkins University, Kavli Institute for the Physics and Mathematics of the Universe (IPMU) / University of Tokyo, the Korean Participation Group, Lawrence Berkeley National Laboratory, Leibniz Institut für Astrophysik Potsdam (AIP), Max-Planck-Institut für Astronomie (MPIA Heidelberg), Max-Planck-Institut für Astrophysik (MPA Garching), Max-Planck-Institut für Extraterrestrische Physik (MPE), National Astronomical Observatories of China, New Mexico State University, New York University, University of Notre Dame, Observatório Nacional / MCTI, The Ohio State University, Pennsylvania State University, Shanghai Astronomical Observatory, United Kingdom Participation Group, Universidad Nacional Autónoma de México, University of Arizona, University of Colorado Boulder, University of Oxford, University of Portsmouth, University of Utah, University of Virginia, University of Washington, University of Wisconsin, Vanderbilt University, and Yale University.

¹ Install (PyPI): <https://pypi.org/project/vice>
Documentation: <https://vice-astro.readthedocs.io>
Source Code: <https://github.com/giganano/VICE.git>

Software: Matplotlib (Hunter 2007); Astropy (Astropy Collaboration et al. 2013, 2018); NumPy (Harris et al. 2020).

6 DATA AVAILABILITY

VICE is open-source software, and the code which computes abundances for our models is publicly available as well. In the GitHub repository, we provide detailed instructions on how to run our models and variations thereof. All observational data appearing in this paper is publicly available, and is also included with the source code for our models and figures.

Appendices

A NORMALIZING THE STAR FORMATION HISTORY

In this appendix, we derive a prescription for calculating the prefactors of an adopted star formation history (SFH) for each annulus in our models. As mentioned in § 2.4, this procedure requires a unitless description of the time-dependence of the SFH in each annulus, denoted $f(t|R_{\text{gal}})$, and a unitless description denoting the radial dependence of the stellar surface density $g(R_{\text{gal}})$. By additionally selecting a total stellar mass of the present day model Galaxy, the solution to the detailed form of the star formation history $\dot{\Sigma}_{\star}(t, R_{\text{gal}})$ is unique. With this approach, we assume that stellar migration does not significantly impact the form of $g(R_{\text{gal}})$, an assumption we demonstrate to be accurate in §2.6.

The surface density of star formation with units of mass per area per time can be expressed in terms of $f(t|R_{\text{gal}})$ as:

$$\dot{\Sigma}_{\star}(t, R_{\text{gal}}) = \dot{\Sigma}_{\star}(t = 0, R_{\text{gal}})f(t|R_{\text{gal}}) \quad (20)$$

and the present-day radial surface density gradient with units of mass per area as:

$$\Sigma_{\star}(R_{\text{gal}}) = \Sigma_{\star}(R_{\text{gal}} = 0)g(R_{\text{gal}}) \quad (21)$$

The integral of $\dot{\Sigma}_{\star}$ with time should yield the surface density gradient at a given radius R_{gal} , up to a prefactor accounting for the return of stellar envelopes to the interstellar medium (ISM):

$$\Sigma_{\star}(R_{\text{gal}}) = (1 - r) \int_0^T \dot{\Sigma}_{\star}(t, R_{\text{gal}}) dt \quad (22a)$$

$$= (1 - r) \dot{\Sigma}_{\star}(t = 0, R_{\text{gal}}) \int_0^T f(t|R_{\text{gal}}) dt \quad (22b)$$

$$\dot{\Sigma}_{\star}(t = 0, R_{\text{gal}}) = \Sigma_{\star}(R_{\text{gal}}) \left[(1 - r) \int_0^T f(t|R_{\text{gal}}) dt \right]^{-1} \quad (22c)$$

$$= \Sigma_{\star}(R_{\text{gal}} = 0)g(R_{\text{gal}}) \left[(1 - r) \int_0^T f(t|R_{\text{gal}}) dt \right]^{-1} \quad (22d)$$

where $(1 - r) \approx 0.6$ is an adequate approximation for a Kroupa IMF (Weinberg et al. 2017, see discussion in their §2.2). This expression relates the two unknowns introduced by equations (20) and (21). We continue by asserting that the integral of the stellar surface density over the area of the disc should be equal to the

present-day stellar mass of the Milky Way:

$$M_{\star}^{\text{MW}} = \int_0^R \Sigma_{\star}(R_{\text{gal}}) 2\pi R_{\text{gal}} dR_{\text{gal}} \quad (23a)$$

$$= \Sigma_{\star}(R_{\text{gal}} = 0) \int_0^R g(R_{\text{gal}}) 2\pi R_{\text{gal}} dR_{\text{gal}} \quad (23b)$$

$$\Sigma_{\star}(R_{\text{gal}} = 0) = M_{\star}^{\text{MW}} \left[\int_0^R g(R_{\text{gal}}) 2\pi R_{\text{gal}} dR_{\text{gal}} \right]^{-1} \quad (23c)$$

Now plugging equation (23c) into equation (22d), and then that into equation (20) yields the desired result:

$$\dot{\Sigma}_{\star}(t, R_{\text{gal}}) = A f(t|R_{\text{gal}}) g(R_{\text{gal}}) \quad (24a)$$

$$A = M_{\star}^{\text{MW}} \left[(1 - r) \int_0^R g(R_{\text{gal}}) 2\pi R_{\text{gal}} dR_{\text{gal}} \int_0^T f(t|R_{\text{gal}}) dt \right]^{-1} \quad (24b)$$

where the upper limits should be the maximum radius of star formation and the end time of the simulation (15.5 kpc and 12.2 Gyr in this paper). This result makes intuitive sense, simply stating that the required normalization of $f(t|R_{\text{gal}})$ is specified by two things: the total stellar mass of the Galaxy and how steep the stellar density falls with increasing radius. As long as the assumption that stellar migration does not significantly alter the form of $g(R_{\text{gal}})$ is not violated, this procedure can be used to calculate prefactors for future models of disc galaxies.

REFERENCES

- Abbott B. P., et al., 2017, *Phys. Rev. Lett.*, **119**, 161101
 Abolfathi B., et al., 2018, *ApJS*, **235**, 42
 Adams S. M., Kochanek C. S., Gerke J. R., Stanek K. Z., Dai X., 2017, *MNRAS*, **468**, 4968
 Ahumada R., et al., 2020, *ApJS*, **249**, 3
 Andrews B. H., Weinberg D. H., Schönrich R., Johnson J. A., 2017, *ApJ*, **835**, 224
 Asplund M., Grevesse N., Sauval A. J., Scott P., 2009, *ARA&A*, **47**, 481
 Astropy Collaboration et al., 2013, *A&A*, **558**, A33
 Astropy Collaboration et al., 2018, *AJ*, **156**, 123
 Basinger C. M., Kochanek C. S., Adams S. M., Dai X., Stanek K. Z., 2020, arXiv e-prints, p. arXiv:2007.15658
 Berg D. A., Skillman E. D., Croxall K. V., Pogge R. W., Moustakas J., Johnson-Groh M., 2015, *ApJ*, **806**, 16
 Berg D. A., Pogge R. W., Skillman E. D., Croxall K. V., Moustakas J., Rogers N. S. J., Sun J., 2020, *ApJ*, **893**, 96
 Bigiel F., Leroy A., Walter F., Blitz L., Brinks E., de Blok W. J. G., Madore B., 2010, *AJ*, **140**, 1194
 Bilitewski T., Schönrich R., 2012, *MNRAS*, **426**, 2266
 Binney J., Tremaine S., 2008, *Galactic Dynamics: Second Edition*
 Bird J. C., Kazantzidis S., Weinberg D. H., Guedes J., Callegari S., Mayer L., Madau P., 2013, *ApJ*, **773**, 43
 Bird J. C., Loebman S. R., Weinberg D. H., Brooks A., Quinn T. R., Christensen C. R., 2020, arXiv e-prints, p. arXiv:2005.12948
 Bland-Hawthorn J., Gerhard O., 2016, *ARA&A*, **54**, 529
 Brooks A. M., Zolotov A., 2014, *ApJ*, **786**, 87
 Brown J. S., et al., 2019, *MNRAS*, **484**, 3785
 Buck T., 2020, *MNRAS*, **491**, 5435
 Buck T., Obreja A., Macciò A. V., Minchev I., Dutton A. A., Ostriker J. P., 2020, *MNRAS*, **491**, 3461
 Case G. L., Bhattacharya D., 1998, *ApJ*, **504**, 761
 Chiappini C., Matteucci F., Gratton R., 1997, *ApJ*, **477**, 765
 Chiappini C., Matteucci F., Romano D., 2001, *ApJ*, **554**, 1044
 Chiappini C., et al., 2015, *A&A*, **576**, L12
 Chieffi A., Limongi M., 2004, *ApJ*, **608**, 405
 Chieffi A., Limongi M., 2013, *ApJ*, **764**, 21

- Chisholm J., Tremonti C., Leitherer C., 2018, *MNRAS*, **481**, 1690
- Christensen C., Quinn T., Governato F., Stilp A., Shen S., Wadsley J., 2012, *MNRAS*, **425**, 3058
- Christensen C. R., Davé R., Brooks A., Quinn T., Shen S., 2018, *ApJ*, **867**, 142
- Clarke A. J., et al., 2019, *MNRAS*, **484**, 3476
- Côté B., et al., 2019, *ApJ*, **875**, 106
- Coulter D. A., et al., 2017, *Science*, **358**, 1556
- Cristallo S., et al., 2011, *ApJS*, **197**, 17
- Daffon S., Cunha K., de la Reza R., Holtzman J., Chiappini C., 2009, *AJ*, **138**, 1577
- de los Reyes M. A. C., Kennicutt Robert C. J., 2019, *ApJ*, **872**, 16
- Drout M. R., et al., 2017, *Science*, **358**, 1570
- Edvardsson B., Andersen J., Gustafsson B., Lambert D. L., Nissen P. E., Tomkin J., 1993, *A&A*, **500**, 391
- Ellison S. L., Lin L., Thorp M. D., Pan H.-A., Scudder J. M., Sanchez S. F., Bluck A. F. L., Maiolino R., 2020a, arXiv e-prints, p. arXiv:2012.04771
- Ellison S. L., Lin L., Thorp M. D., Pan H.-A., Sanchez S. F., Bluck A. F. L., Belfiore F., 2020b, arXiv e-prints, p. arXiv:2012.04772
- Ertl T., Janka H. T., Woosley S. E., Sukhbold T., Ugliano M., 2016, *ApJ*, **818**, 124
- Feuillet D. K., et al., 2018, *MNRAS*, **477**, 2326
- Feuillet D. K., Frankel N., Lind K., Frinchaboy P. M., García-Hernández D. A., Lane R. R., Nitschelm C., Roman-Lopes A. r., 2019, *MNRAS*, **489**, 1742
- Frankel N., Rix H.-W., Ting Y.-S., Ness M., Hogg D. W., 2018, *ApJ*, **865**, 96
- Frankel N., Sanders J., Ting Y.-S., Rix H.-W., 2020, *ApJ*, **896**, 15
- Fraternali F., Tomassetti M., 2012, *MNRAS*, **426**, 2166
- Frinchaboy P. M., et al., 2013, *ApJ*, **777**, L1
- Gaia Collaboration et al., 2018, *A&A*, **616**, A1
- García-Benito R., et al., 2017, *A&A*, **608**, A27
- García Pérez A. E., et al., 2016, *AJ*, **151**, 144
- Gerke J. R., Kochanek C. S., Stanek K. Z., 2015, *MNRAS*, **450**, 3289
- González Delgado R. M., et al., 2014, *A&A*, **562**, A47
- Grand R. J. J., et al., 2017, *MNRAS*, **467**, 179
- Grand R. J. J., et al., 2018, *MNRAS*, **474**, 3629
- Griffith E., Johnson J. A., Weinberg D. H., 2019, *ApJ*, **886**, 84
- Griffith E., et al., 2020, arXiv e-prints, p. arXiv:2009.05063
- Grisoni V., Spitoni E., Matteucci F., Recio-Blanco A., de Laverny P., Hayden M., Mikolaitis Š., Worley C. C., 2017, *MNRAS*, **472**, 3637
- Guesten R., Mezger P. G., 1982, *Vistas in Astronomy*, **26**, 159
- Harris C. R., et al., 2020, *Nature*, **585**, 357
- Hayden M. R., et al., 2014, *AJ*, **147**, 116
- Hayden M. R., et al., 2015, *ApJ*, **808**, 132
- Haywood M., 2008, *MNRAS*, **388**, 1175
- Hekker S., Johnson J. A., 2019, *MNRAS*, **487**, 4343
- Holmberg J., Nordström B., Andersen J., 2007, *A&A*, **475**, 519
- Holoien T. W. S., et al., 2019, *MNRAS*, **484**, 1899
- Holtzman J. A., et al., 2015, *AJ*, **150**, 148
- Hunter J. D., 2007, *Computing in Science & Engineering*, **9**, 90
- Isern J., 2019, *ApJ*, **878**, L11
- Johnson J. A., 2019, *Science*, **363**, 474
- Johnson J. W., Weinberg D. H., 2020, *MNRAS*, **498**, 1364
- Kalberla P. M. W., Kerp J., 2009, *ARA&A*, **47**, 27
- Kalirai J. S., Hansen B. M. S., Kelson D. D., Reitzel D. B., Rich R. M., Richer H. B., 2008, *ApJ*, **676**, 594
- Kennicutt Robert C. J., 1998, *ApJ*, **498**, 541
- Kennicutt R. C., Evans N. J., 2012, *ARA&A*, **50**, 531
- Kennicutt Robert C. J., de los Reyes M. A. C., 2020, arXiv e-prints, p. arXiv:2012.05363
- Khoperskov S., Haywood M., Snaith O., Di Matteo P., Lehnert M., Vasiliev E., Naroenkov S., Berczik P., 2021, *MNRAS*, **501**, 5176
- Kroupa P., 2001, *MNRAS*, **322**, 231
- Krumholz M. R., Burkhardt B., Forbes J. C., Crocker R. M., 2018, *MNRAS*, **477**, 2716
- Kubryk M., Prantzos N., Athanassoula E., 2013, *MNRAS*, **436**, 1479
- Lacey C. G., Fall S. M., 1985, *ApJ*, **290**, 154
- Law D. R., Majewski S. R., 2010, *ApJ*, **714**, 229
- Leahy D. A., Wu X., 1989, *PASP*, **101**, 607
- Leroy A. K., Walter F., Brinks E., Bigiel F., de Blok W. J. G., Madore B., Thornley M. D., 2008, *AJ*, **136**, 2782
- Leroy A. K., et al., 2013, *AJ*, **146**, 19
- Licquia T. C., Newman J. A., 2015, *ApJ*, **806**, 96
- Liu L., Gao Y., Greve T. R., 2015, *ApJ*, **805**, 31
- Loebman S. R., Roškar R., Debattista V. P., Ivezić Ž., Quinn T. R., Wadsley J., 2011, *ApJ*, **737**, 8
- Loebman S. R., Ivezić Ž., Quinn T. R., Governato F., Brooks A. M., Christensen C. R., Jurić M., 2012, *ApJ*, **758**, L23
- Loebman S. R., et al., 2014, *ApJ*, **794**, 151
- Lyne A. G., Manchester R. N., Taylor J. H., 1985, *MNRAS*, **213**, 613
- Madau P., Dickinson M., 2014, *ARA&A*, **52**, A15
- Majewski S. R., et al., 2017, *AJ*, **154**, 94
- Maoz D., Graur O., 2017, *ApJ*, **848**, 25
- Maoz D., Mannucci F., 2012, *Publ. Astron. Soc. Australia*, **29**, 447
- Martig M., et al., 2016, *MNRAS*, **456**, 3655
- Matteucci F., Francois P., 1989, *MNRAS*, **239**, 885
- Melioli C., Brighenti F., D’Ercole A., de Gouveia Dal Pino E. M., 2008, *MNRAS*, **388**, 573
- Melioli C., Brighenti F., D’Ercole A., de Gouveia Dal Pino E. M., 2009, *MNRAS*, **399**, 1089
- Minchev I., Famaey B., Combes F., Di Matteo P., Mouhcine M., Wozniak H., 2011, *A&A*, **527**, A147
- Minchev I., Famaey B., Quillen A. C., Di Matteo P., Combes F., Vlajić M., Erwin P., Bland-Hawthorn J., 2012, *A&A*, **548**, A126
- Minchev I., Chiappini C., Martig M., 2013, *A&A*, **558**, A9
- Minchev I., Chiappini C., Martig M., 2014, *A&A*, **572**, A92
- Minchev I., Steinmetz M., Chiappini C., Martig M., Anders F., Matijević G., de Jong R. S., 2017, *ApJ*, **834**, 27
- Mishenina T., Pignatari M., Gorbaneva T., Bisterzo S., Travaglio C., Thielemann F. K., Soubiran C., 2019, *MNRAS*, **484**, 3846
- Mor R., Robin A. C., Figueras F., Roca-Fàbrega S., Luri X., 2019, *A&A*, **624**, L1
- Nidever D. L., et al., 2014, *ApJ*, **796**, 38
- Nidever D. L., et al., 2015, *AJ*, **150**, 173
- Noguchi M., 2018, *Nature*, **559**, 585
- Nordström B., Andersen J., Holmberg J., Jørgensen B. R., Mayor M., Pont F., 2004a, *Publ. Astron. Soc. Australia*, **21**, 129
- Nordström B., et al., 2004b, *A&A*, **418**, 989
- Palla M., Matteucci F., Spitoni E., Vincenzo F., Grisoni V., 2020, *MNRAS*, **498**, 1710
- Peek J. E. G., 2009, *ApJ*, **698**, 1429
- Pejcha O., Thompson T. A., 2015, *ApJ*, **801**, 90
- Pian E., et al., 2017, *Nature*, **551**, 67
- Pinsonneault M. H., et al., 2014, *ApJS*, **215**, 19
- Radburn-Smith D. J., et al., 2012, *ApJ*, **753**, 138
- Recio-Blanco A., et al., 2014, *A&A*, **567**, A5
- Rojas-Arriagada A., et al., 2017, *A&A*, **601**, A140
- Romano D., Karakas A. I., Tosi M., Matteucci F., 2010, *A&A*, **522**, A32
- Roškar R., Debattista V. P., Stinson G. S., Quinn T. R., Kaufmann T., Wadsley J., 2008a, *ApJ*, **675**, L65
- Roškar R., Debattista V. P., Quinn T. R., Stinson G. S., Wadsley J., 2008b, *ApJ*, **684**, L79
- Ruiz-Lara T., Gallart C., Bernard E. J., Cassisi S., 2020, *Nature Astronomy*, **4**, 965
- Sánchez S. F., 2020, *ARA&A*, **58**, 99
- Schönrich R., Binney J., 2009, *MNRAS*, **396**, 203
- Sellwood J. A., Binney J. J., 2002, *MNRAS*, **336**, 785
- Sharma S., Hayden M. R., Bland-Hawthorn J., 2020, arXiv e-prints, p. arXiv:2005.03646
- Siegel D. M., 2019, *European Physical Journal A*, **55**, 203
- Silva Aguirre V., et al., 2018, *MNRAS*, **475**, 5487
- Spitoni E., Recchi S., Matteucci F., 2008, *A&A*, **484**, 743
- Spitoni E., Matteucci F., Recchi S., Cescutti G., Pipino A., 2009, *A&A*, **504**, 87

- Spitoni E., Vincenzo F., Matteucci F., Romano D., 2016, *MNRAS*, **458**, 2541
- Spitoni E., Matteucci F., Jönsson H., Ryde N., Romano D., 2018, *A&A*, **612**, A16
- Spitoni E., Silva Aguirre V., Matteucci F., Calura F., Grisoni V., 2019, *A&A*, **623**, A60
- Spitoni E., Verma K., Silva Aguirre V., Calura F., 2020, *A&A*, **635**, A58
- Spitoni E., et al., 2021, arXiv e-prints, p. [arXiv:2101.08803](https://arxiv.org/abs/2101.08803)
- Sukhbold T., Ertl T., Woosley S. E., Brown J. M., Janka H. T., 2016, *ApJ*, **821**, 38
- Tacconi L. J., et al., 2018, *ApJ*, **853**, 179
- van de Voort F., Pakmor R., Grand R. J. J., Springel V., Gómez F. A., Marinacci F., 2020, *MNRAS*, **494**, 4867
- Vincenzo F., Kobayashi C., 2020, *MNRAS*, **496**, 80
- Vincenzo F., Weinberg D. H., Miglio A., Lane R. R., Roman-Lopes A., 2021a, arXiv e-prints, p. [arXiv:2101.04488](https://arxiv.org/abs/2101.04488)
- Vincenzo F., Thompson T. A., Weinberg D. H., Griffith E. J., Johnson J. W., Johnson J. A., 2021b, arXiv e-prints, p. [arXiv:2102.04920](https://arxiv.org/abs/2102.04920)
- Wadsley J. W., Keller B. W., Quinn T. R., 2017, *MNRAS*, **471**, 2357
- Wang L., Dutton A. A., Stinson G. S., Macciò A. V., Penzo C., Kang X., Keller B. W., Wadsley J., 2015, *MNRAS*, **454**, 83
- Weinberg D. H., Andrews B. H., Freudenburg J., 2017, *ApJ*, **837**, 183
- Weinberg D. H., et al., 2019, *ApJ*, **874**, 102
- Wielen R., Fuchs B., Dettbarn C., 1996, *A&A*, **314**, 438
- Zolotov A., et al., 2012, *ApJ*, **761**, 71